

## CHAOTIC COLD ACCRETION ON TO BLACK HOLES IN ROTATING ATMOSPHERES

M. GASPARI<sup>1</sup>, M. RUSZKOWSKI<sup>2,3</sup>, S. PENG OH<sup>4</sup>, F. BRIGHENTI<sup>5</sup>, P. TEMI<sup>6</sup>

<sup>1</sup>Max Planck Institute for Astrophysics, Karl-Schwarzschild-Strasse 1, 85741 Garching, Germany; mgaspari@mpa-garching.mpg.de

<sup>2</sup>Department of Astronomy, University of Michigan, 500 Church Street, Ann Arbor, MI 48109, USA

<sup>3</sup>Michigan Institute for Research in Astrophysics, University of Michigan, Ann Arbor, MI 48104, USA

<sup>4</sup>Department of Physics, University of California, Santa Barbara, CA 93106, USA

<sup>5</sup>Astronomy Department, University of Bologna, Via Ranzani 1, 40127 Bologna, Italy

<sup>6</sup>Astrophysics Branch, NASA/Ames Research Center, MS 245-6, Moffett Field, CA 94035

*Draft version April 17, 2019*

### ABSTRACT

The fueling of black holes is one key problem in the evolution of baryons in the universe. In previous work, we showed that chaotic cold accretion dramatically differs from classic gas accretion based on Bondi theory. Using 3D high-resolution hydrodynamic simulations, we now probe the impact of *rotation* on the hot and cold accretion flow in a typical massive galaxy. In the hot mode (when cooling or heating are negligible), the pressure-dominated flow forms a geometrically thick rotational barrier, suppressing the black hole accretion rate to about 1/3 of the spherical case value. Stirring the hot flow with subsonic turbulence results in similar suppression due to the local generation of vorticity. When radiative cooling is dominant, the gas loses pressure support against gravity and quickly circularizes in a cold thin disk. The accretion rate is low and decoupled from the cooling rate, albeit its level is higher than in the hot mode due to the gas condensation. In the more common state of a turbulent and heated atmosphere (where average cooling is quenched), chaotic cold accretion drives the dynamics as long as the gas velocity dispersion exceeds the rotational velocity, i.e. turbulent Taylor number  $Ta_t < 1$ . Extended multiphase filaments condense out of the hot phase via thermal instability and rain toward the black hole, boosting the accretion rate up to 100 times the Bondi rate ( $\dot{M}_\bullet \sim \dot{M}_{\text{cool}}$ ). Initially, turbulence broadens the angular momentum distribution of the hot gas, allowing the cold phase to condense with prograde or retrograde motion. Subsequent chaotic collisions between cold filaments, clouds, and a clumpy variable torus promote the cancellation of angular momentum, leading to high accretion rates. As turbulence weakens ( $Ta_t > 1$ ), the broadening of the distribution and the efficiency of collisions diminish, damping the accretion rate  $\propto Ta_t^{-1}$ , until the cold disk dominates the gas dynamics. This is exacerbated by the increased difficulty to grow nonlinear thermal instability in a halo dominated by rotation, as radial compression is inhibited by the centrifugal force. We propose the following cycle regulating the gaseous halos of massive galaxies, groups, and clusters. As gas begins to cool, chaotic cold accretion develops and boosts feedback heating. The cold mode is then reduced and the rotating disk remains the sole cold structure ( $Ta_t > 1$ ). Its consumption leaves the atmosphere in hot mode, which strongly suppresses accretion and feedback, allowing the cycle to start again.

*Keywords:* accretion – black hole physics – hydrodynamics – galaxies: ISM, IGM, ICM – instabilities – turbulence – methods: numerical

### 1. INTRODUCTION & OBSERVATIONS

In current astrophysics, a marked disconnection exists between theoretical works focusing on the vicinity of supermassive black holes (SMBHs) and those studying the large-scale properties of the host (a massive elliptical, galaxy group or cluster). The former often employ idealized, constant boundary conditions, while the latter are forced to rely on semi-analytic subgrid models. The intermediate zone, between a few 10 kpc of the host galaxy and the sub-pc core, is however a crucial region which often determines the fueling and feeding of the black hole.

In Gaspari et al. 2013b (hereafter GRO13), we aimed to fill this gap, showing that realistic turbulence, cooling, and heating affecting the hot gaseous halo, can dramatically change the accretion flow on to black holes, departing from the idealized picture of Bondi (1952) formula. As the cooling time becomes relatively low compared with the dynamical time ( $t_{\text{cool}} \lesssim 10 t_{\text{ff}}$ ), cold clouds and filaments condense out of the hot phase via nonlinear thermal instability (TI). Chaotic collisions promote the funneling of the cold phase toward the BH, leading to episodic spikes in the accretion rate up to  $\sim 100\times$  the Bondi rate. In poetic terms, chaotic cold accretion (CCA)

can be viewed as ‘raining on to black holes’.

The simplicity of the Bondi formula makes it tempting to be exploited in theoretical and observational studies (e.g. Reynolds et al. 1996; Loewenstein et al. 2001; Churazov et al. 2002; Baganoff et al. 2003; Di Matteo et al. 2003, 2005; Springel et al. 2005; Allen et al. 2006; Croton et al. 2006; Hopkins et al. 2006; Rafferty et al. 2006; Cattaneo & Teyssier 2007; Sijacki et al. 2007; Hardcastle et al. 2007; McCarthy et al. 2008; Booth & Schaye 2009; Cattaneo et al. 2009; Barai et al. 2014; Fujita et al. 2014; Nemmen & Tchekhovskoy 2014). Knowing the black hole mass  $M_\bullet$  and the gas entropy at large radii ( $K \propto T/\rho^{\gamma-1}$ , where  $\gamma$  is the adiabatic index,  $\rho$  the gas density, and  $T$  the gas temperature) allows us to immediately retrieve the accretion rate via

$$\dot{M}_B = \lambda 4\pi (GM_\bullet)^2 \frac{\rho_\infty}{c_{s,\infty}^3} \propto K_\infty^{-3/2}, \quad (1)$$

where  $\lambda$  is a factor of order unity (varying as a function of  $\gamma$  and the accretor radius; GRO13, sec. 1). However, Eq. 1 can only be used if the hydrodynamic flow is adiabatic (no heating or cooling), unperturbed, spherically symmetric,

with steady boundary conditions at infinity. If one of these conditions is violated, then Bondi derivation and formula can not be applied. Bondi himself warns in the first line of his 1952 abstract that he investigates a special accretion problem. In the last decade, observations and simulations of gas in galaxies, groups, and clusters have proven that atmospheres are turbulent (e.g. Norman & Bryan 1999; Schuecker et al. 2004; Dolag et al. 2005; Kim & Ryu 2005; Nagai et al. 2007; Churazov et al. 2008; Lau et al. 2009; Vazza et al. 2009; Borgani & Kravtsov 2011; Ruszkowski & Oh 2010, 2011; de Plaa et al. 2012; Sanders & Fabian 2013; Gaspari & Churazov 2013; Banerjee & Sharma 2014; Gaspari et al. 2014b; similarly for the interstellar medium, Elmegreen & Scalo 2004), while continuously shaped by the competition of cooling and heating processes (e.g. Vikhlinin et al. 2006; McNamara & Nulsen 2007, 2012; Diehl & Statler 2008; Rasmussen & Ponman 2009; Sun et al. 2009; Gaspari et al. 2014a). It is thus essential to adopt physical models of black hole accretion.

Tracking the proper accretion rate and dominant mode of SMBHs is fundamental in order to understand and model the impact of AGN ('active galactic nucleus') feedback. The energy released by a SMBH can reach  $10^{62}$  erg, which is able to affect not only the host galaxy but also the surrounding group/cluster gaseous halo (e.g. Gaspari et al. 2011a,b, 2012a,b). AGN feedback can indeed solve many astrophysical problems as heating cooling flows, quenching star formation, forming buoyant bubbles and shocks, or ejecting metals and low-entropy gas at large radii (Gaspari et al. 2013a for a brief review). SMBHs are thus the thermostats regulating the baryonic structures throughout the cosmic evolution.

In recent times, it has become clear that most – if not all – massive systems retain a gaseous halo down to galaxies with stellar masses  $M_* \sim 10^{11} M_\odot$  (Anderson et al. 2013 and 2014 in prep.; Planck Collaboration et al. 2013, Fig. 4), including spirals (e.g. Anderson & Bregman 2011; Dai et al. 2012). Therefore, cold gas condensation and accretion is expected to play central role in the evolution of SMBHs and their host galaxies, as also supported by other works (Quataert & Narayan 2000; Pizzolato & Soker 2005; Soker 2006; Soker et al. 2009; Barai et al. 2012; Mathews & Guo 2012). Interestingly, high-redshift galaxies may not even necessitate of condensation, since they can directly accrete cold gas through cosmic-web inflows triggered by large-scale disk instabilities and tidal torques (e.g. Dekel et al. 2009; Hopkins & Quataert 2010, 2011). Chaotic collisions via minor mergers may also facilitate accretion, as shown by King & Pringle (2006, 2007) and Nayakshin & King (2007; sec. 8 in GRO13 for a review).

Observations of multiphase gas ( $T < 10^6$  K) in massive galaxies have exponentially grown through the last decade, detecting extended ionized gas in optical H $\alpha$ + [NII] (Heckman et al. 1989; Macchetto et al. 1996; Crawford et al. 1999; McDonald & Veilleux 2009; McDonald et al. 2010, 2011, 2012; Werner et al. 2014), which is typically cospatial with infrared H $_2$  (e.g. Jaffe et al. 2005; Hatch et al. 2005; Wilman et al. 2009, 2011; Oonk et al. 2010), molecular gas traced by CO (Lim et al. 2000; Edge 2001; Salomé & Combes 2003; Salomé et al. 2008; Hamer et al. 2014), far-infrared [CII], [OI] (Mittal et al. 2012; Werner et al. 2013), and far-ultraviolet CIV, OVI (Bregman et al. 2006; Sparks et al. 2012). These data strongly favor the scenario of in-situ condensation via TI, as opposed to gas stripping from infalling galaxies. Recently, the unprecedented resolution

and sensitivity of ALMA has further proven the central role of condensed cold gas in the form of clouds, turbulent disks, and outflows (David et al. 2014; McNamara et al. 2014; Russell et al. 2014). Remarkably, most cool-core systems with  $t_{\text{cool}} < 1$  Gyr contain filamentary multiphase gas (Cavagnolo et al. 2008; Rafferty et al. 2008) and central radio sources (Mittal et al. 2009), indicating that the cooling gas is the main driver of AGN feedback. The increase of radio-loud AGN with more massive halos (Best et al. 2007), which have higher cooling rates (Shabala et al. 2008) and slower rotation, further support the fueling via CCA. It shall be noted that molecular gas does not necessitate to be correlated, or better, cospatial with AGN bubbles or jets/outflows (e.g. Werner et al. 2014), since CCA quickly consumes the free-falling cold gas; powerful AGN feedback can also drag it out of the galaxy (e.g. Canning et al. 2013).

After GRO13 initial study, many features of the newly proposed CCA remain to be tackled, in this and future investigations. One important open question concerns the role of rotation in being able to suppress accretion, in combination with cooling, heating, and turbulence (see also Proga & Begelman 2003; Krumholz et al. 2005, 2006; Pizzolato & Soker 2010; Hobbs et al. 2011; Narayan & Fabian 2011). Current surveys using integral-field spectroscopy (Emsellem et al. 2007, 2011) show that early type galaxies display slow or fast rotating stellar kinematics, likely reflecting separate formation and evolution histories. While low-luminosity galaxies are typically fast rotators, massive galaxies (as brightest cluster/group galaxies), the focus of the present work, belong to the 'slow' rotator family (e.g. Jimmy et al. 2013; Kormendy et al. 2009 for a review). Recurrent gas-poor (dry) mergers (e.g. Bois et al. 2011) or AGN outflows (e.g. Gaspari et al. 2012b) can both contribute in reducing angular momentum. Slow rotator/massive ellipticals have angular momentum parameter  $\lambda_{R_e} \sim 0.1 - 0.3$  (Emsellem et al. 2007), corresponding to stellar rotational velocities  $v_{*,\text{rot}} \sim 0.1 - 0.3 \sigma_*$  (Binney et al. 1990; Caon et al. 2000; Pinkney et al. 2003; Jimmy et al. 2013). A notable example with significant rotation is NGC 4649.

Compared with the stellar kinematics, the rotation of the gas in observed massive ellipticals is more uncertain. Roughly 70% of the hot gas within the effective radius likely comes from stellar mass loss (e.g. Brighenti & Mathews 1999), thereby gas rotation is expected to share similar specific angular momentum as the local stars,  $v_{\text{rot}} \sim 0.1 - 0.3 \sigma_*$  (e.g. Caon et al. 2000). Evidence for gas rotation in the inner part of the galaxy is given by the X-ray ellipticity, typically  $\lesssim 0.2$ , which steadily declines below that of the stars at  $r \gtrsim 1$  kpc (Diehl & Statler 2007; Brighenti et al. 2009). The negative slope of the X-ray ellipticity is typically moderate (Diehl & Statler 2007), suggesting that transport processes – as turbulence – are required to circularize the isophotes and to prevent the rapid spin-up of the gas due to cooling flows (e.g. Brighenti & Mathews 1996, 2000). Non-zero gas angular momentum can be also associated with subsonic sloshing motions and cold fronts due to infalling substructures (Markevitch & Vikhlinin 2007; ZuHone et al. 2013) or with the galaxy peculiar velocity (e.g. Zabludoff et al. 1993).

As in GRO13, we intend to perform controlled astrophysical experiments, dissecting each physics in a methodical way, in order to properly disentangle its relative impact on the hot and cold accretion flow affected by rotation. In §2, we describe the physical and numerical ingredients of the simulations. In §3, we study the rotating flow in the purely adia-

batic, galactic atmosphere. In §4, we analyze the importance of cooling, inducing a cold thin disk. §5 shows the impact of realistic 3D turbulence in the rotating hot flow. In §6, we combine cooling and stirring, while in §7 we present the complete chaotic cold accretion evolution in a rotating halo, including heating and varying levels of turbulence. In §8, we summarize and discuss our findings in the context of AGN feedback and observations. Remarkably, CCA results to be unhindered as long as a key dimensionless quantity, which we define as ‘turbulent Taylor’<sup>1</sup> number, remains below unity:

$$\text{Ta}_t \equiv \frac{v_{\text{rot}}}{\sigma_v} < 1, \quad (2)$$

where  $v_{\text{rot}}$  and  $\sigma_v$  are the rotational velocity and turbulent velocity dispersion of the gas, respectively.

## 2. PHYSICS & NUMERICS

The implemented physics and numerics are described in depth in GRO13 (sec. 2), to which the reader is referred for further details. Here we summarize the essential features and new ingredients, as rotation.

### 2.1. Initial conditions & rotation

We study the accretion flow in a typical massive elliptical galaxy (NGC 5044) embedded in the gaseous intragroup medium. The initial temperature and gravitational potential profiles are unchanged compared with our previous work. The  $T$  profile is directly derived from *Chandra/XMM* observations (Gaspari et al. 2011b). The total static potential  $\phi$  is provided by the central SMBH ( $M_\bullet = 3 \times 10^9 M_\odot$ ), the galactic stellar component ( $M_* \simeq 3.4 \times 10^{11} M_\odot$ , with effective radius  $\simeq 10$  kpc), and a dark matter NFW halo with virial mass  $M_{\text{vir}} \simeq 3.6 \times 10^{13} M_\odot$  (with concentration  $c \simeq 9.5$ ). Schwarzschild and Bondi radii are  $R_S \equiv 2GM_\bullet/c^2 \simeq 3 \times 10^{-4}$  pc and  $r_B \equiv GM_\bullet/c_{s,\infty}^2 \simeq 85$  pc, respectively (the sound speed is  $c_{s,\infty} \simeq 390$  km s<sup>-1</sup> near 1 kpc). We integrate the system for a long-term evolution,  $\sim 200 t_B$ , where  $t_B \equiv r_B/c_{s,\infty} \simeq 210$  kyr.

The density profile is retrieved from hydrostatic equilibrium (neglecting the black hole). In this study, we test the gas rotation, which induces a centrifugal force, effectively lowering the gravitational acceleration  $g$  along  $R \equiv (x^2 + y^2)^{1/2}$ . This partially changes the stratification of the hot gaseous halo. The new hydrostatic equilibrium can be better visualized and setup separating the two main directions,  $R$  and  $z$ :

$$\frac{\partial}{\partial R} \ln \rho = - \left( \frac{\partial \phi}{\partial R} - \frac{v_{\text{rot}}^2}{R} \right) c_{s,i}^{-2} - \frac{\partial}{\partial R} \ln T, \quad (3)$$

$$\frac{\partial}{\partial z} \ln \rho = - \frac{\partial \phi}{\partial z} c_{s,i}^{-2} - \frac{\partial}{\partial z} \ln T, \quad (4)$$

where  $c_{s,i}^2 = k_b T / \mu m_p$  is the isothermal sound speed (the atomic weight is  $\mu \simeq 0.62$ ). As customary (e.g. Strickland & Stevens 2000), the rotational velocity of the gas is parametrized as a fraction of the circular velocity

$$v_{\text{rot}}(R) \equiv e_{\text{rot}} v_{\text{circ}}(R, 0) = e_{\text{rot}} \left( R \frac{\partial \phi(R, 0)}{\partial R} \right)^{1/2}, \quad (5)$$

<sup>1</sup> This quantity shares similarity with classic Taylor number, which characterizes the importance of centrifugal forces relative to viscous forces:  $\text{Ta} = \omega^2 R^4 / \nu^2$ , where  $\omega$  is the angular velocity,  $R$  is the cylindrical radius, and  $\nu$  is the kinematic viscosity. Notice that  $\text{Ta} \propto \text{Ta}_t^2$ .

where  $e_{\text{rot}}$  is a free parameter ranging between 0 and 1, the latter corresponding to full rotational support. We first integrate the hydrostatic equilibrium along  $R$  (Eq. 3), then along the  $z$  direction (Eq. 4), linearly interpolating the retrieved 2D matrix in the discretized 3D domain. The central density normalization is the same as in GRO13. The initial profiles are shown in Fig. 1c. As suggested by observations, the resultant rotational velocity is fairly constant with  $R$  (outside the Keplerian influence region of the SMBH); at 26 kpc  $v_{\text{rot}}$  is just  $\sim 30\%$  higher than at 1 kpc. Using constant specific angular momentum at large radii ( $v_{\text{rot}} \propto R^{-1}$ ) should be thus avoided as initial condition.

We discuss now the reference  $e_{\text{rot}}$ . The Jeans equation for a spherically symmetric, isotropic stellar system in equilibrium can be written as

$$v_{*,\text{rot}}^2 - \sigma_{*,r}^2 \left( \frac{\partial \ln \rho_*}{\partial \ln r} + \frac{\partial \ln \sigma_{*,r}^2}{\partial \ln r} \right) = v_{\text{circ}}^2. \quad (6)$$

Neglecting rotation, the radial stellar velocity dispersion for our simulated galaxy peaks at  $\sigma_{*,r} \simeq 230$  km s<sup>-1</sup> (the 3D velocity dispersion is  $\sigma_* = \sqrt{3} \sigma_{*,r}$ ). For weak rotation, the stellar velocity dispersion is a good proxy for the circular velocity. Massive elliptical galaxies are known to have irregular velocity profiles, at best with mild coherent rotation, in particular for the gas component (e.g. Caon et al. 2000). As discussed in §1, gas rotation can typically reach  $v_{\text{rot}} \lesssim 0.3 \sigma_*$ . In order to maximize the impact of rotation, we thus adopt  $e_{\text{rot}} = 0.3$  as reference, leading to an average gas rotational velocity  $v_{\text{rot}} \approx 100$  km s<sup>-1</sup> ( $r \sim 1 - 13$  kpc). Adopting slower rotation has negligible impact on the CCA dynamics, resembling GRO13 models, as  $v_{\text{rot}} \ll \sigma_v$ . Since faster rotation flattens too much the density profile and isophotes (§1), it is better to compare models with fixed  $e_{\text{rot}}$  and varying  $\sigma_v$  (the cooling rate also remains the same), albeit  $\text{Ta}_t$  defines the self-similar dynamics in both cases (§7).

### 2.2. Hydrodynamics & source terms

We use a modified version of the adaptive-mesh-refinement code FLASH4 (Fryxell et al. 2000) to integrate the equations of hydrodynamics, adopting an exceptionally large dynamical range. The maximum resolution is  $\sim 0.8$  pc, with static zoom-in toward the center. The box width reaches 52 kpc ( $\sim 600 r_B$ ), an extension of almost a factor  $10^5$  (see GRO13 for further details on resolution and convergence). Notice that using  $e_{\text{rot}} = 0.3$  implies that the circularization radius is  $r_{\text{circ}} = (v_{\text{rot}}/v_{\text{circ}}) r_{\text{init}} = 0.3 r_{\text{init}}$ . Even considering the steepening of  $v_{\text{circ}}$  due to the SMBH potential ( $\sim 4000$  km s<sup>-1</sup> at 1 pc), we can resolve circular motions down to a few 10 pc. TI form up to several kpc, hence we will be able to clearly assess if the cold gas is accreted or circularizes (see the thin disk evolution in §4).

In addition to hydrodynamics, we add the source terms related to the black hole sink, turbulence driving, radiative cooling, and distributed heating (GRO13), testing step by step the contribution of each physics to the accretion process. Using the pseudo-relativistic Paczyński & Wiita (1980) BH potential, the sonic point (for adiabatic index  $\gamma = 5/3$ ) is not located at  $r = 0$ , but at a finite distance near the pc scale. This justifies the use of a central gas sink region of a few cells (which avoids artificial overpressure bounces), since the internal region is causally disconnected.

Turbulence is implemented via a spectral forcing scheme, based on an Ornstein-Uhlenbeck random process, which

drives a time-correlated and zero-mean acceleration field, reproducing experimental high-order structure functions (Fisher et al. 2008). The source of turbulence can be galaxy motions, substructure mergers, supernovae or AGN feedback (e.g. Norman & Bryan 1999; Lau et al. 2009; Vazza et al. 2009; Gaspari et al. 2012b). We keep the subsonic turbulent velocity used in GRO13 as reference,  $\sigma_v \sim 150 \text{ km s}^{-1}$  (3D Mach number  $\text{Ma} \sim 0.35$ ), stirring the gas at injection scales  $L \gtrsim 4 \text{ kpc}$ . Adopting  $e_{\text{rot}} = 0.3$ , the reference turbulent model has Taylor number  $\text{Ta}_t \sim 0.7$ . In §5-7, we test weaker turbulence, i.e.  $\text{Ta}_t = 1.5$  and 3. Turbulent heating (with timescale  $\propto \text{Ma}^{-2}$ ) is subdominant during our entire evolution. Even with stratification, the power spectrum of turbulence follows the classic Kolmogorov slope (Gaspari et al. 2014b).

The hot plasma cools via X-ray radiation mainly due to Bremsstrahlung at  $T \gtrsim 10^7 \text{ K}$  and line emission at lower temperature. The radiative emissivity is  $\mathcal{L} = n_e n_i \Lambda$ , where  $n_e$  and  $n_i$  are the electron and ion number density, respectively. The cooling function  $\Lambda(T)$  is modeled following Sutherland & Dopita (1993), adopting solar metallicity. The stable cold phase has a temperature floor at  $10^4 \text{ K}$  (possibly preserved by heating due to hot young stars, photoemission of UV-irradiated dust grains, the central AGN, and/or cosmic rays – Bakes & Tielens 1994; McDonald & Veilleux 2009 for a discussion). The initial ratio of the cooling time,  $t_{\text{cool}} \equiv 1.5 nk_B T / n_e n_i \Lambda$ , and free-fall time,  $t_{\text{ff}} \equiv (2r/g)^{1/2}$  has a minimum  $\sim 4\text{-}5$  near 250 pc. As  $t_{\text{cool}}/t_{\text{ff}} < 10$  thermal instability can grow nonlinearly (Gaspari et al. 2012a; McCourt et al. 2012; Sharma et al. 2012; for other studies on TI see Field 1965; Krolik & London 1983; Balbus & Soker 1989; Pizzolato & Soker 2005).

AGN feedback, in conjunction with stellar heating and mergers (e.g. Brighenti & Mathews 2003; Gaspari et al. 2011a,b; Barai et al. 2014), acts to maintain the cool core of galaxies, groups, and clusters in global thermal quasi-equilibrium ( $\lesssim 10$  percent), preserving core temperatures at  $\sim 1/3$  of the virial temperature (e.g. Vikhlinin et al. 2006; Diehl & Statler 2008; Rasmussen & Ponman 2009; Sun et al. 2009). We do not model AGN outflows or jets as in Gaspari et al. (2012a,b), since computationally unfeasible. In the final models (§7), we inject distributed heating, mimicking a post-outburst phase, when the feedback heating has been properly deposited (Gaspari et al. 2012a, Fig. 9). Computationally, we set the heating rate (per unit volume) to be equal to the average radiative emissivity in finite radial shells,  $\mathcal{H} \approx \langle \mathcal{L} \rangle$ .

### 3. ADIABATIC ACCRETION

Following the structure presented in GRO13, we test step by step the impact of each physical process. We begin analyzing the model purely based on hydrodynamics. No cooling, heating, or turbulence is affecting the accretion flow. The adiabatic flow shares tight connection with Bondi (1952) accretion, albeit the spherical symmetry is broken by the initial gas rotation ( $e_{\text{rot}} = 0.3$ , i.e.  $v_{\text{rot}} \approx 100 \text{ km s}^{-1}$ ; §2.1).

#### 3.1. Accretion rate

In Fig. 1a, we show the main diagnostic, the temporal evolution of the accretion rate during 40 Myr ( $\sim 200 t_B$ ). The impact of rotation (solid line; top) is to suppress the accre-

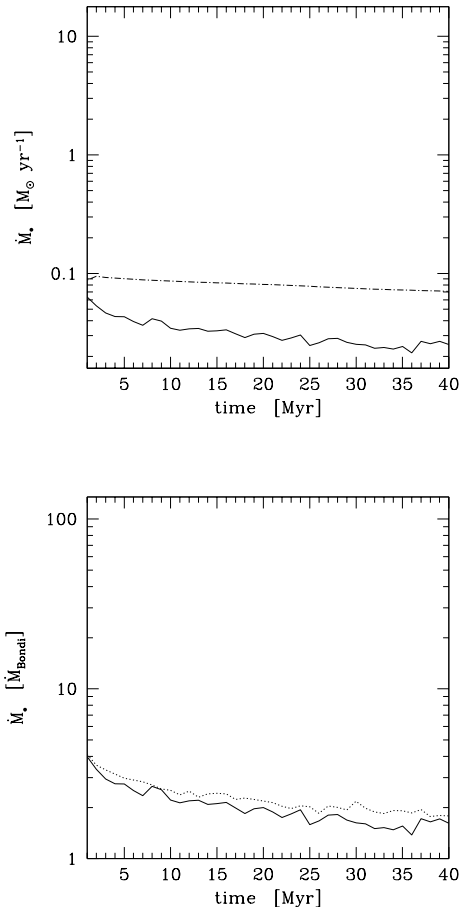


**Figure 1a.** Adiabatic rotating accretion: evolution of the accretion rate (1 Myr average). Top: accretion rate in  $M_{\odot} \text{ yr}^{-1}$  units, for the rotating ( $e_{\text{rot}} = 0.3$ ; solid) and non-rotating atmosphere (dot-dashed; see GRO13). Bottom: Accretion rate normalized to the run-time Bondi rate (averaged over  $r \sim 1\text{-}2 \text{ kpc}$  as in large-scale simulations) for the reference rotation  $e_{\text{rot}} = 0.3$  (solid) and  $e_{\text{rot}} = 0.15$  (dotted). The central rotational barrier forming within  $r_B$  suppresses accretion typically by  $\sim 3$  compared with the spherically symmetric accretion flow.

tion rate by a factor  $\sim 3$  compared with the non-rotating atmosphere (dashed line; sec. 3.1 in GRO13), reaching  $\dot{M}_{\bullet} \simeq 0.025 M_{\odot} \text{ yr}^{-1}$ . The average rate is slightly decreasing due to the presence of the galactic gradients, progressively altering the ‘boundary’ conditions near a few  $r_B$  ( $\dot{M}_B \propto K_{\infty}^{-3/2}$ ; the Bondi boundary conditions at infinity have no meaning in stratified atmospheres). Ignoring this minor trend, the accretion rate is solely stifled by the central rotationally-supported barrier, reaching a statistical steady state in a few  $10 t_B$ .

In the bottom panel (Fig. 1a), the accretion rate is normalized to the Bondi rate (Eq. 1), averaged over  $r \sim 1\text{-}2 \text{ kpc}$ , as customarily employed in large-scale/cosmological simulations. Comparing the reference run with  $e_{\text{rot}} = 0.3$  (solid) and the model with  $e_{\text{rot}} = 0.15$  (dotted) indicates that the final accretion rate is weakly lowered with increasing rotation. Interestingly, adopting the Bondi formula at large radii predicts a fairly consistent accretion rate. Therefore, boosting the Bondi accretion rate by a large factor ( $\sim 100$ ; e.g. Di Matteo et al. 2005; Booth & Schaye 2009) is not required, even if  $r_B$  is under-resolved, at least in the regime of

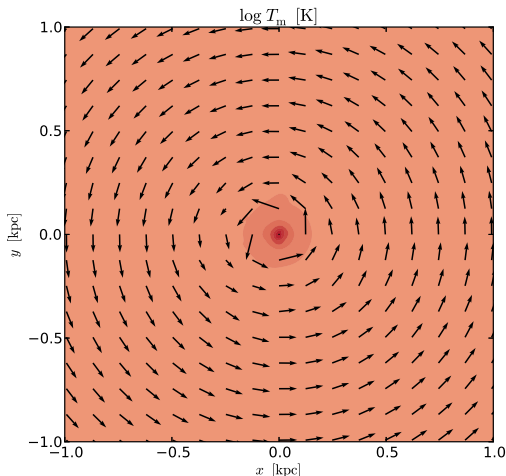


**Figure 1b.** Adiabatic accretion with  $e_{\text{rot}} = 0.3$ :  $x$ - $y$  rotational plane cross-section (central  $2 \text{ kpc}^2$ ) of the mass-weighted temperature at final time; the normalization of the velocity field is  $2000 \text{ km s}^{-1}$  (this unit arrow is  $1/8$  of the image width). The gas progressively circularizes toward the equatorial plane, stifling accretion. Within the Bondi radius, the pressure-supported toroidal structure is variable, experiencing recurrent mild expansions and contractions, thus forming the pinwheel configuration.

a hot and rotating atmosphere (a similar conclusion applies in the presence of turbulence, but not if cooling is dominant).

### 3.2. Dynamics

The suppression of accretion is related to the formation of a central toroidal structure, where gas with relatively high angular momentum circularizes, further blocking part of the inflow solid angle. The hot gas can only accrete along the polar funnel perpendicular to the equatorial ( $x$ - $y$ ) plane. The circulation within the toroidal region is variable, as reflected by the mild oscillations in  $\dot{M}_\bullet$ . The configuration is partially unstable: the polar flow is inflowing, while the equatorial region is partially outflowing or circulating, leading to recurrent expansions and contractions (Fig. 1b).

The ‘pinwheel’ and toroidal configuration, as well as the suppression of the accretion rate, are consistent with the results of Proga & Begelman (2003) and Krumholz et al. (2005), although our flow is embedded in galactic gradients. For low/moderate vorticity as in our typical system (hot plasma in most galaxies has subsonic and sub-Keplerian velocities<sup>2</sup>), the accretion rate is weakly dependent on the initial angular momentum (Fig. 1a, bottom), since the suppression in the final stage is related to the geometrically thick toroidal structure, which eventually builds up with similar shape. Its typical radius is the BH influence radius  $\sim r_B$  with height  $H \sim r_B$  – for a Keplerian disk  $H = c_s/\omega = (r^3/r_B)^{1/2}$ . The polar funnel can be thus approximated as a cone with half-opening angle  $\theta \sim \pi/4$ , allowing gas accretion within a solid angle  $\Omega = 2\pi(1 - \cos\theta) \simeq 1.84$ . Considering the two cones, the funnel has  $\Omega \sim 1/3$  of the spherical solid angle, broadly consistent with the simulated  $\dot{M}_\bullet$  suppression (Fig. 1a, top).

<sup>2</sup> If the gas velocities are super Keplerian near  $r_B$ , accretion is driven by the action of shock dissipation allowing the gas to become bound; in this regime, the higher the vorticity the lower  $\dot{M}_\bullet$ , typically with a very small and stable torus (cf. Krumholz et al. 2005).

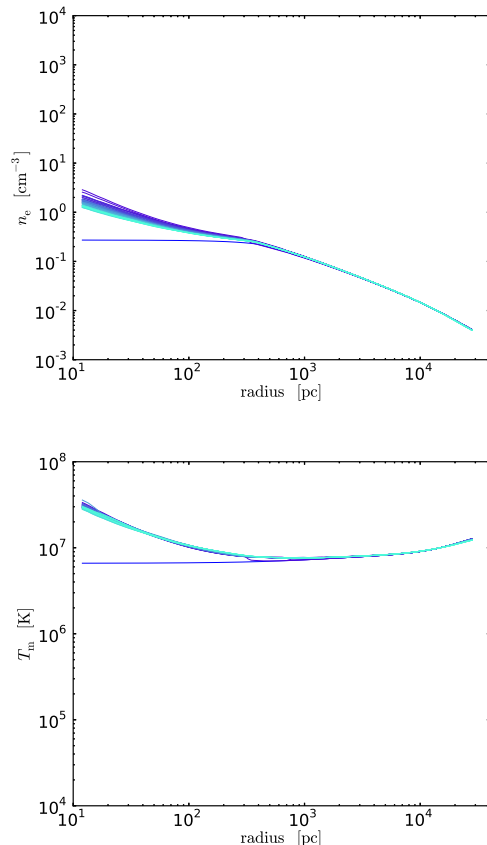


**Figure 1c.** Adiabatic accretion with  $e_{\text{rot}} = 0.3$ : evolution of the mass-weighted electron density (top) and temperature (bottom) radial profiles, sampled every 1 Myr (from dark blue to cyan). The cuspy profiles are similar to the classic Bondi solution (GRO13), smoothly joining the galactic gradients at large  $r$ .

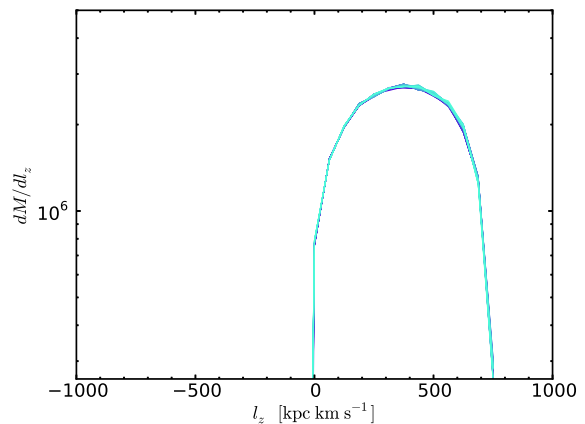


**Figure 1d.** Adiabatic accretion with  $e_{\text{rot}} = 0.3$ : mass ‘probability’ distribution function (PDF) per bin of specific angular momentum along the rotation axis  $z$  ( $M_\odot$  per  $\text{kpc km s}^{-1}$ ), for the gas within  $r < 8 \text{ kpc}$ . The color coding is the same as for the radial profiles (Fig. 1c), covering 40 Myr. With no additional physics, the system overall preserves the initial angular momentum distribution (coherent counter-clockwise rotation).

### 3.3. Radial profiles and $l_z$ distribution

In Fig. 1c, we show the mass-weighted radial profiles of electron gas density  $n_e$  (top) and temperature  $T_m$  (bottom), sampled every 1 Myr (dark blue to cyan color). The cuspy profiles are similar to the classic Bondi solution (e.g.  $T \propto r^{-1}$ ; GRO13), smoothly joining the galactic gradients at large radii. The slight central  $n_e$  decrease partly occurs due to the variable boundary conditions near  $r_B$ , and partly due to rotation. Since the hot flow is mainly dominated by pressure, the toroidal region has large height ( $H = c_s/\omega$ ) and is smooth, without a net demarcation line as in the radiative run forming a cold thin disk (§4). The X-ray emission-weighted profiles (not shown) are not dissimilar due to the absence of the cold phase. Therefore, X-ray observations would see peaked gas temperature in the nucleus of the galaxy, if the hot mode is the currently dominant regime of accretion (typically occurring after AGN feedback has overheated the system; §8).

In Fig. 1d, we present another important diagnostic: the mass distribution function (PDF) of specific angular momentum along the rotation axis  $l_z$ , during the 40 Myr evolution. Since the model has no heating, cooling, or turbulence, and the accretion is substantially inhibited, the system overall conserves the angular momentum distribution. Notice that the PDF of  $l_z$  has only positive values, the mark of coherent counter-clockwise rotation (the right tail is decreasing since we consider the gas within  $r < 8$  kpc). Reshaping the angular momentum distribution via other physical processes is crucial to trigger boosted accretion.

## 4. ACCRETION WITH COOLING

In the next model, the reference rotating accretion flow experiences cooling due to radiation (mainly Bremsstrahlung in the X-ray band and line cooling below 1 keV) with emissivity  $\mathcal{L} = n_e n_i \Lambda(T)$ . No source of heating or turbulence affects the dynamics.

### 4.1. Accretion rate

The central result is the decoupling between the accretion rate and the cooling rate (Fig. 2a, top), no more closely tracking each other as in the spherically symmetric cooling flow (GRO13; sec. 4). The dense gas quickly loses pressure support via radiative emission (initial minimum  $t_{\text{cool}}$  is  $\sim 8$  Myr) and forms a rotationally-supported thin disk. The fast condensation affects first the inner and denser gas with lower angular momentum, which can be quickly accreted ( $\dot{M}_\bullet \simeq 0.5 M_\odot \text{ yr}^{-1}$ ). After 10 Myr, the cold phase arises from the hot gas with high angular momentum. Falling from  $r > r_B$  toward the center, this cooling gas rapidly increases the rotational velocity and circularizes, damping the accretion rate. At final time,  $\dot{M}_\bullet \simeq 0.15 M_\odot \text{ yr}^{-1}$  (blue) and  $\dot{M}_{\text{cool}} \simeq 15 M_\odot \text{ yr}^{-1}$  (dashed), a difference of two orders of magnitude. The normalized accretion rate is also low, roughly four times the Bondi rate at the kpc scale.

Compared with the adiabatic run (solid black), the accretion rate is about  $6\times$  higher, since the weakened pressure support increases the effective inflow, in particular along the polar region. The presence of a condensing hot halo thus alters the classic thin disk picture, where the cold gas is the only entity.

### 4.2. Dynamics

Figure 2b shows the formation of the symmetric thin disk in more detail. The hot gas loses internal energy and thus pres-

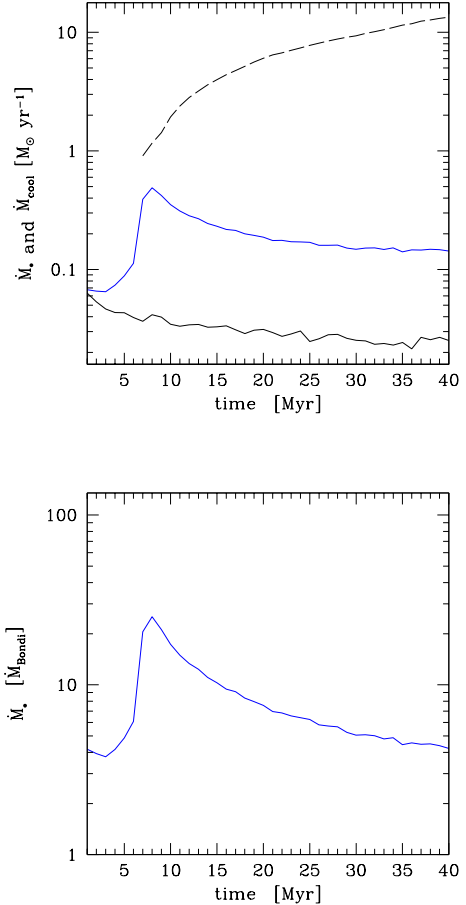


**Figure 2a.** Accretion with cooling and  $\epsilon_{\text{rot}} = 0.3$  (blue): evolution of the accretion rate (physical and normalized to the kpc-scale, run-time Bondi rate – top and bottom panel, respectively). The dashed line is the average cooling rate (related to the gas with  $T < 10^5$  K). Solid black line is the adiabatic rotating model (§3). Despite the substantial cooling rates,  $\dot{M}_{\text{cool}} \sim 15 M_\odot \text{ yr}^{-1}$ , the final accretion rate is two orders of magnitude lower due to the formation of a rotationally-supported thin disk.

sure, but it is still balanced by rotation along  $R$ , leading to the infall toward the direction perpendicular to the  $x$ - $y$  plane, where the low-entropy gas finds a new rotational equilibrium. Due to the steep multiphase stratification and transonic inflow, the disk experiences hydrodynamical instabilities, as Kelvin-Helmoltz and Rayleigh-Taylor. The overall picture is very different from a spherically symmetric cooling flow (GRO13), since  $\dot{M}_\bullet \ll \dot{M}_{\text{cool}}$ . Along the polar funnel, the transonic flow is not inhibited by rotation and gas can quickly accrete.

Massive galaxies which are dominated by cooling (weak or no heating), are thus expected to show a rotationally supported cold disk, arising from the fast spin-up of the gas. The X-ray ellipticity greater than that of the stellar component in the inner 1 kpc may be a sign of this phenomenon (e.g. NGC 4649; cf. Brighenti et al. 2009), albeit moderate turbulence is still required in order to avoid markedly flat isophotes inconsistent with observations (Diehl & Statler 2007; see also Brighenti & Mathews 2000).

It is interesting to note that the disk is internally turbulent, even without magneto-rotational instability

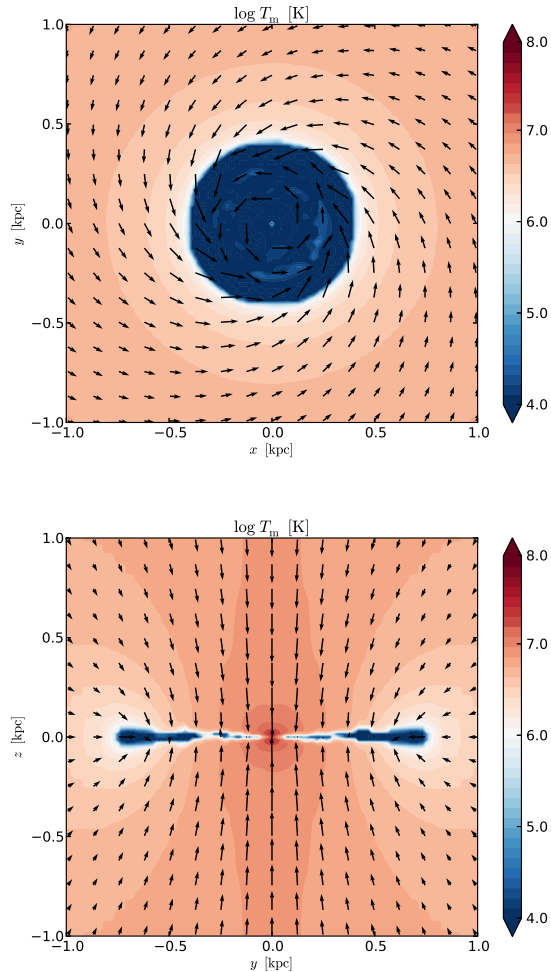


**Figure 2b.** Accretion with cooling and  $\epsilon_{\text{rot}} = 0.3$ : temperature cross-sections ( $2 \text{ kpc}^2$ ) through  $z = 0$  (top) and  $x = 0$  (bottom), after 2 and 4  $t_{\text{cool}}$ , respectively. The velocity field normalization is  $6000 \text{ km s}^{-1}$  (this unit arrow is 1/8 of the image width). The maps show the formation of a symmetric cold thin disk, which quickly condenses out of the hot phase and stifles accretion.

(Balbus & Hawley 1998) due to the interaction with the hot phase at the condensation layer (Fig. 2b). Near the accretor, this is crudely comparable to a Shakura & Sunyaev (1973) alpha parameter of the order of  $\sim 0.05$  (an analog of the disk Mach number). We notice that, in the stirred runs, the injected turbulence ( $\text{Ma} \sim 0.1\text{-}0.3$ ) always exceeds this value.

#### 4.3. Radial profiles and $l_z$ distribution

The mass-weighted radial profiles in Fig. 2c reveal the presence of the highly dense ( $10^3 \text{ cm}^{-3}$ ) and cold thin disk, condensed out of the hot atmosphere. At variance with  $T_m$ , the X-ray temperature (bottom) has only a mild decline from large to 1 kpc radius, where it starts to stabilize around  $10^7 \text{ K}$ . The cold disk keeps growing through time due to the continuous condensation of higher angular momentum gas. The rotating structure is thin, with slightly expanding dense lobes where the warm gas is still condensing ( $H = c_s/\omega$ ; Fig. 2b), which can be tracked in the profiles.

The disk extends to  $\sim 1 \text{ kpc}$  after 40 Myr of evolu-

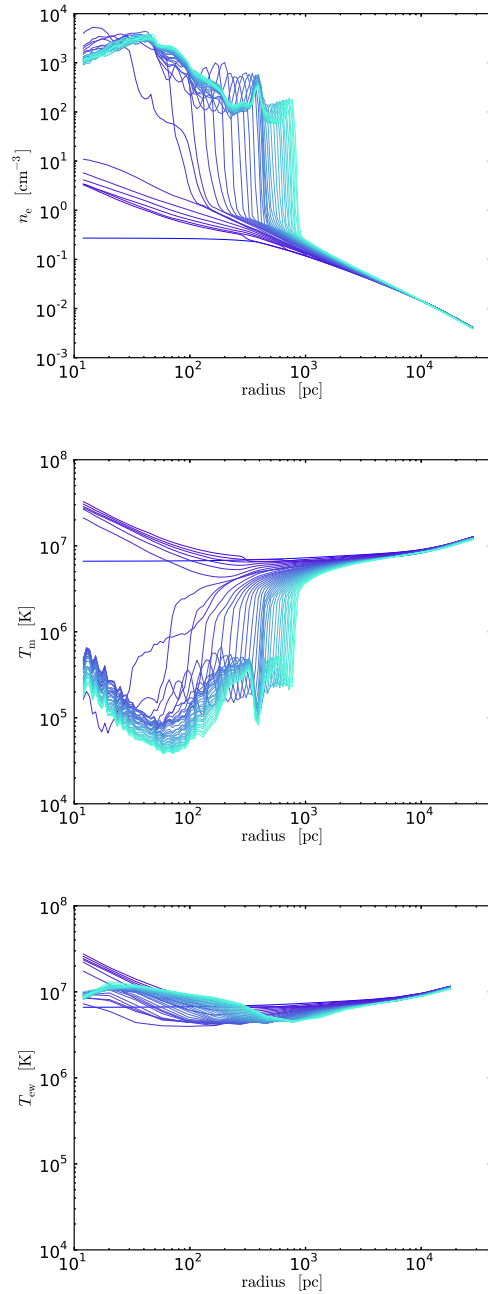


**Figure 2c.** Accretion with cooling and  $\epsilon_{\text{rot}} = 0.3$ : 3D mass- and emission-weighted radial profiles of density and temperature (cf. Fig. 1c). The  $T_{\text{ew}}$  profile has X-ray threshold of 0.3 keV and is computed in larger radial bins (emulating a *Chandra* observation). The cold thin disk keeps growing via condensation. The X-ray temperature is overall insensitive to the presence of the cold disk.

tion, with its size starting to saturate as the cooling rate (Fig. 2a). During periods of weak heating and turbulence, this could be a common regime, allowing to develop the rotating cold disks observed in many massive elliptical galaxies (Mathews & Brighenti 2003; Young et al. 2011; Alatalo et al. 2013; NGC 6868 and NGC 7049, Werner et al. 2014). The retrieved size of the disk (e.g. via ALMA or *Herschel*) may point out how long the cooling-dominated phase has lasted, setting constraints on the AGN feedback duty cycle (albeit we

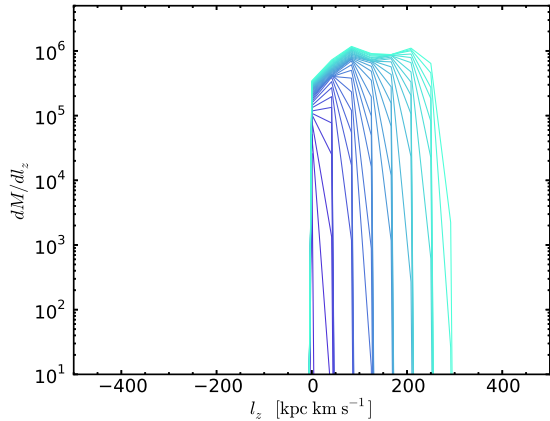


**Figure 2d.** Accretion with cooling and  $e_{\text{rot}} = 0.3$ : mass PDF per bin of specific angular momentum  $l_z$ , for the cold phase (full evolution from blue to cyan lines). The PDF of the hot phase is analogous to that shown in Fig. 1d, albeit shifting by  $\sim 15$  percent to higher normalization and  $l_z$ . The cold phase emerges out of this distribution, adding during time higher  $l_z$  gas, and thus widening the PDF.

note that a clumpy rotational structure can be present during CCA and significant feedback; §7).

Figure 2d shows the  $l_z$  distribution of the cold phase. The PDF of the hot phase is analogous to that in Fig. 1d, shifting by  $\sim 15$  percent to higher normalization and  $l_z$  due to the large-scale inflow of gas losing pressure. The cold phase emerges out of the hot gas distribution, progressively accumulating higher  $l_z$  gas coming from larger radii, and thus widening the PDF while the disk grows (blue to cyan). As in the previous adiabatic run,  $l_z$  is only positive, the mark of coherent rotation, albeit now in the form of a cold thin disk. Again, such a distribution of angular momentum implies substantially suppressed  $\dot{M}_\bullet$ .

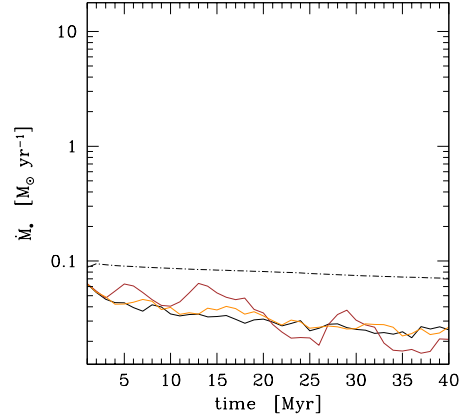
## 5. ADIABATIC ACCRETION WITH TURBULENCE

Cosmic systems are rarely (if ever) in perfect hydrostatic equilibrium. The hot gas in galaxies, groups, and clusters is continuously stirred by the action of AGN/supernovae feedback, galaxy motions, and mergers. We thus probe the effect of turbulence on the rotating and adiabatic flow, testing intrinsic<sup>3</sup> velocity dispersion in the range of  $\sigma_v \sim 40 - 150 \text{ km s}^{-1}$ .

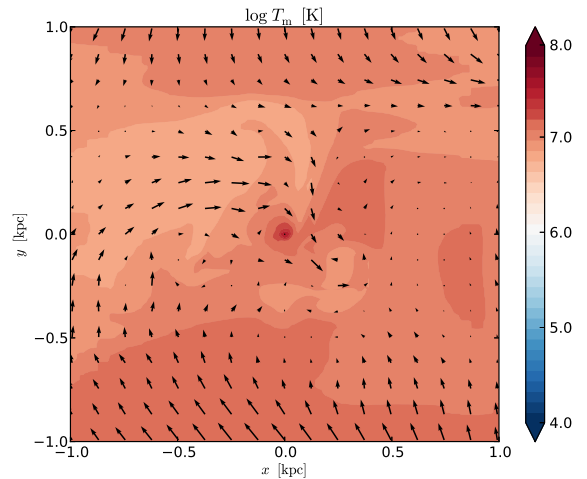
### 5.1. Accretion rate and dynamics

Figure 3a shows the evolution of the accretion rate for the reference  $\text{Ma} \sim 0.35$  (brown) and for 1/4 lower Mach number ( $\text{Ta}_t \sim 3$ ; orange). In both runs, the suppression of  $\dot{M}_\bullet$  is  $\sim 1/3$  compared with the non-rotating Bondi flow (dashed line; see also GRO13). Remarkably, the suppression is analogous to that retrieved in the purely rotating run (black; §3). While turbulence with  $\sigma_v > v_{\text{rot}}$  is able to disrupt the coherent rotation and to prevent the full circularization, its basic action is to transport momentum. No total angular momentum is created. However, turbulence *locally* induces prograde or retrograde vorticity (Fig. 3c), via eddies generated during the Kolmogorov cascade. The (subsonic) turbulent

<sup>3</sup> The rotational velocity can be cleanly removed calculating the mean in cylindrical coordinates,  $v_{\text{rot}} = -v_x y/R + v_y x/R$ .



**Figure 3a.** Adiabatic accretion with subsonic turbulence and  $e_{\text{rot}} = 0.3$  (brown:  $\text{Ma} \sim 0.35$ , i.e.  $\text{Ta}_t \sim 0.75$ ; orange: 1/4 lower Mach number, i.e.  $\text{Ta}_t \sim 3$ ): evolution of the accretion rate. The accretion rate is suppressed by a factor of  $\sim 3$  compared with the non-rotating model (dot-dashed), as in the purely rotating run (solid black; §3), since turbulence still induces local (but not global) vorticity. The chaotic eddies generate however higher variability, as long as  $\text{Ta}_t < 1$ . In the opposite regime, rotation drives the dynamics.



**Figure 3b.** Adiabatic accretion with subsonic turbulence (reference  $\text{Ma} \sim 0.35$ ) and  $e_{\text{rot}} = 0.3$ : mid-plane temperature cut (cf. Fig. 1b). The equatorial plane does not display coherent rotation, since the gas can not properly circularize in the presence of significant turbulence ( $\sigma_v > v_{\text{rot}}$ ). The central vortical motions stifle again accretion.

accretion flow is thus analogous to a gradually varying rotating flow near the accretor (Fig. 3b). As discussed in §3, for a pressure-supported and slowly rotating flow, the geometric funnel where the gas can accrete is roughly invariant, linked to a suppression of  $\sim 1/3$ . The central spiraling motion is enhanced by the baroclinic instability due to the atmosphere stratification (Krumholz et al. 2006). We note for subsonic turbulence, local vorticity is more relevant than the gas bulk motion relative to the accretor. For the reference  $\text{Ma} \sim 0.35$ , the  $\dot{M}_\bullet$  suppression related to the bulk motion (Bondi & Hoyle 1944) is just  $\propto (1 + M^2)^{-3/2} \simeq 0.84$ .

A difference with the purely rotating, adiabatic flow is the

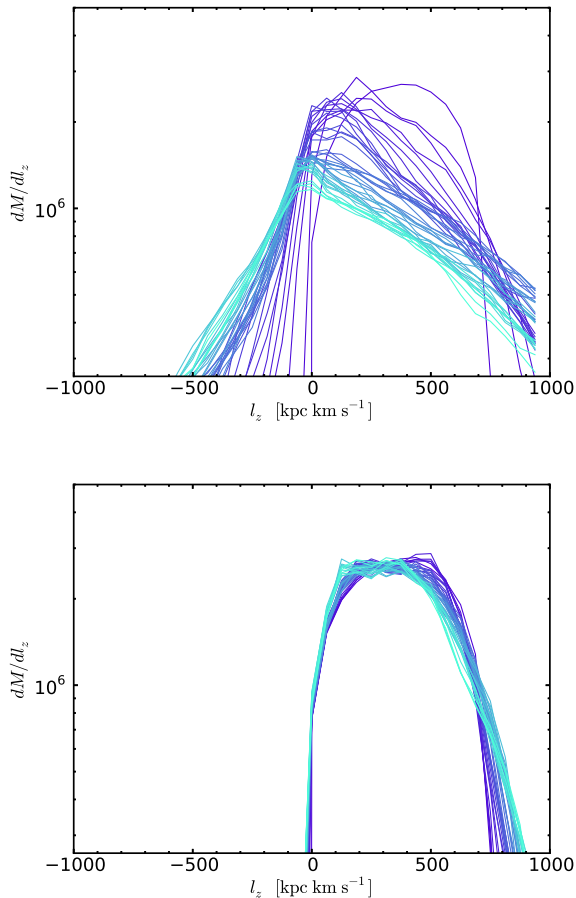


**Figure 3c.** Adiabatic accretion with subsonic turbulence (top:  $Ma \sim 0.35$ ; bottom: 1/4 lower Mach number, i.e.  $Ta_t \sim 3$ ) and  $e_{rot} = 0.3$ : mass PDF per bin of specific angular momentum  $l_z$ , for the gas within  $r < 8$  kpc (cf. Fig. 1d). If  $Ta_t < 1$ , turbulence widens the PDF, inducing both retrograde and prograde motions. In the opposite regime,  $Ta_t > 1$ , turbulence is too weak to induce retrograde motions: the underlying counter-clockwise rotation remains overall intact, with minor fluctuations superimposed.

increased  $\dot{M}_\bullet$  variability. The turbulent eddies randomly have low or high angular momentum, generating the peaks and valleys observed in the accretion rate, which oscillate by a factor of  $\sim 2$ . The key role of the local eddy is remarked by the turbulent run with no rotation presented in GRO13 (sec. 6), showing similarly suppressed  $\dot{M}_\bullet$ . As  $Ta_t > 1$  (Fig. 3a; orange), the flow is however driven by coherent rotation, with only minor turbulent perturbations, thereby reverting to the evolution described in §3.

### 5.2. $l_z$ distribution and radial profiles

The importance of the  $Ta_t \equiv v_{rot}/\sigma_v \sim 1$  threshold can be better appreciated in the distribution of angular momentum (Fig. 3c). If  $Ta_t < 1$  (top), stirring can substantially reshape  $PDF(l_z)$ . Turbulence can be approximated as a diffusion process (with diffusivity  $\sim \sigma_v L$ ; Gaspari & Churazov 2013), spreading linear and thus<sup>4</sup> angular momentum (effective viscosity). The initially peaked and solely positive  $l_z$  distribution is progressively morphed into a broader PDF including negative values, with variance  $\propto \sigma_v$ . The PDF is

<sup>4</sup> The radial displacement has uniformly random distribution.

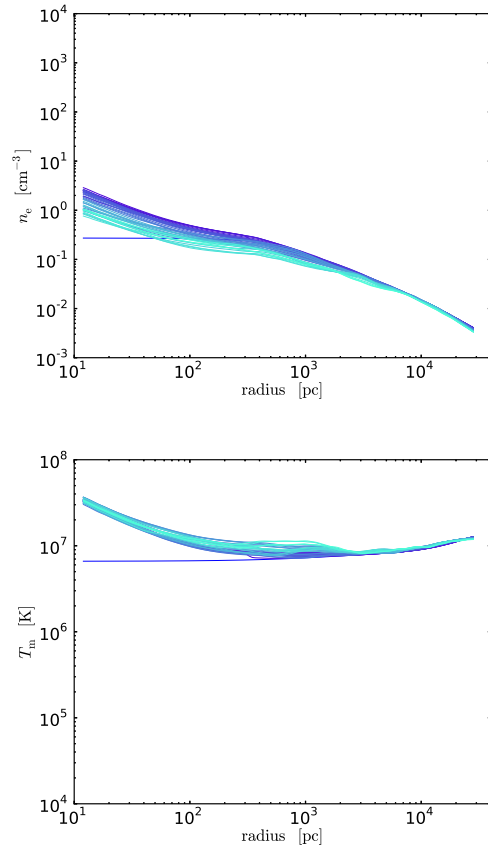


**Figure 3d.** Adiabatic accretion with subsonic turbulence ( $Ma \sim 0.35$  and  $e_{rot} = 0.3$ ): mass-weighted profiles of density and temperature (cf. Fig. 1c). The profiles are cuspy, as in the classic Bondi flow, albeit becoming progressively shallower due to turbulent diffusion (dissipative heating is negligible, as remarked by the large-scale  $T$  profile).

skewed toward the right tail due to the initial rotation. In the  $\sigma_v \gg v_{rot}$  regime, the PDF would be symmetric around zero.

It is relevant to note that the end product of real viscosity is a homogeneous velocity (Dirac delta PDF), while the steady state of turbulence is always local perturbations ( $\propto \sigma_v$ ). Turbulent diffusion not only acts on momentum, but also on  $K$ ,  $\rho$ ,  $T$ , as shown by the gradually shallower radial profiles (Fig. 3d), and by the power spectrum analysis presented in Gaspari et al. (2014b). The fact that turbulence mimics a transport mechanism, while inducing significant local fluctuations, is a key element to develop chaotic cold accretion (§7). Notice that, by itself, the broadening of the angular momentum distribution does not stimulate boosted accretion. In contrast to the cold clouds experiencing major inelastic collisions, the hot diffuse halo is in global hydrostatic equilibrium due to the pressure support, thereby the subsonic eddies do not mostly cancel angular momentum.

In the opposite regime  $Ta_t > 1$  (Fig. 3c, bottom), turbulence is too weak to induce retrograde motions: the underlying counter-clockwise  $l_z$  distribution remains overall intact and the coherent rotation drives the dynamics. The reduced effective diffusivity is also evident in the radial profiles (not shown), where the central density decreases only to  $n_e \simeq 1.5 \text{ cm}^{-3}$ .

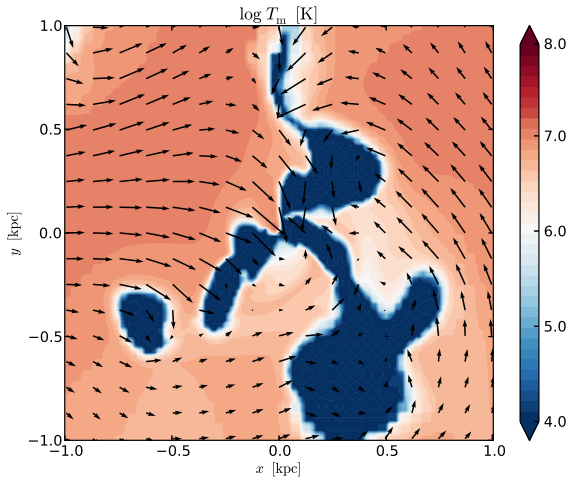


**Figure 4a.** Accretion with cooling, turbulence ( $Ma \sim 0.35$ ), and  $e_{\text{rot}} = 0.3$ : mid-plane  $T_m$  cross-section through  $z = 0$  (final time). Without heating, the system experiences a massive CCA flow. Extended cold filaments and clouds condense out of the hot phase via TI, and through recurrent chaotic collisions are quickly accreted by the BH. No steady thin disk can be formed.

## 6. ACCRETION WITH COOLING & TURBULENCE

In the next model, we turn on radiative cooling, while the reference subsonic turbulence ( $Ma \sim 0.35$ ) stirs the hot atmosphere. The development of a clumpy multiphase medium completely changes the behavior of accretion. This simulation also warns how mild chaotic motions can profoundly modify the picture presented by simple analytic models (e.g. the classic thin disk).

### 6.1. Dynamics

In Fig. 4a, the temperature map reveals the absence of major coherent motions. No source of heating is present, nevertheless the perturbations seeded by subsonic turbulence grow nonlinearly via thermal instability and produce cold filamentary structures. The dynamics of the gas is chaotic, driven by multiple collisions in the inner region. Collision means the major interaction between two distinct elements (clouds, filaments, or clumpy torus), allowing to substantially cancel angular momentum (see also Nayakshin & King 2007; Pizzolato & Soker 2010) and thus to boost the accretion rate. On top of turbulent diffusion, collisions promote further disruption of coherent motions and rotating structures. No steady thin disk can be formed (compare with §4), although at later times a volatile and clumpy cold torus emerges out of the residual gas with large  $l_z$  due to incomplete cancellation (§6.3).

The main point is that the multiphase gas halo in galaxies should be treated as a collisional, hydrodynamical system. The cold phase is not well described by ballistic orbits. The collisions are more frequent in the inner 1 kpc core, as major filaments have length comparable to this radius, initiating further interactions between cold elements. The cold phase retains the imprint of the hot phase at condensation, but collisions drive its dynamics in the subsequent stage.

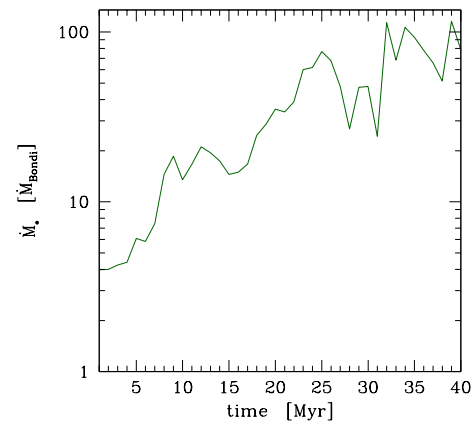
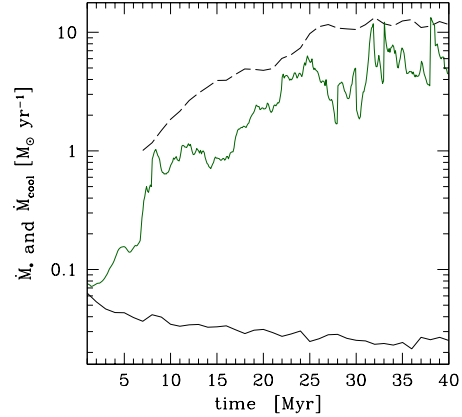


**Figure 4b.** Accretion with cooling, turbulence ( $Ma \sim 0.35$ ), and  $e_{\text{rot}} = 0.3$  (green): evolution of the physical and normalized accretion rate (cf. Fig. 2a; the average of  $\dot{M}_\bullet$  in the top panel has 0.1 Myr step). The dashed line is the average cooling rate (1 Myr step). Chaotic cold accretion drives the dynamics, in similar manner as found in GRO13 (as long as  $Ta < 1$ ). Recurrent collisions in the cold phase cancel angular momentum and boost the accretion rate up to two orders of magnitude with respect to the Bondi rate. The accretion rate is again linearly tied to  $\dot{M}_{\text{cool}}$ .

### 6.2. Accretion rate

Chaotic cold accretion drives the dynamics, in similar manner as found in GRO13 (as long as  $Ta_t < 1$ ; see next §7). The cold clouds condense out of the stirred hot phase, thereby experiencing chaotic streamlines. The rapid prograde versus retrograde collisions cancel angular momentum, and consequently boost the accretion rate up to two orders of magnitude with respect to the kpc-scale Bondi rate (Fig. 4b, bottom). Compared with the adiabatic run (either turbulent or rotating; solid black, top), the increase is almost a factor  $10^3$ . At variance with the thin disk evolution (§4), the accretion rate is linearly tied to  $\dot{M}_{\text{cool}}$  (dashed), albeit experiencing substantial chaotic variability up to  $\sim 1$  dex. The cooling rate saturates slightly faster around  $15 M_\odot \text{ yr}^{-1}$  due to the turbulent mixing of entropy. At  $t > 25$  Myr (top), the residual cold gas with high  $l_z > 0$  induces deeper  $\dot{M}_\bullet$  valleys (via a clumpy torus).

Needless to say, this regime with no heating produces unrealistically high cooling rates and condensation. X-ray observations indicate  $\dot{M}_{\text{cool}}$  lower by at least an order of magnitude (e.g. Tamura et al. 2003; Peterson & Fabian 2006

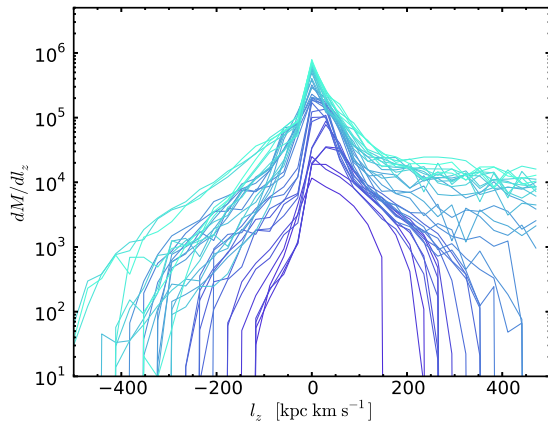


**Figure 4c.** Accretion with cooling, turbulence ( $Ma \sim 0.35$ ), and  $e_{\text{rot}} = 0.3$ : mass PDF per bin of specific angular momentum  $l_z$ , for the cold phase (the hot phase has PDF analogous to Fig. 3c, top). At variance with the purely radiative run, the cold phase randomly condenses out of a broad  $l_z$  distribution, including both prograde and retrograde motions. This permits frequent major collisions, canceling angular momentum. The mass of unaccreted cold gas tends to significantly rise with time due to the unheated cooling flow.

for a review). Nevertheless, it is instructive to understand chaotic cold accretion embedded in a pure cooling flow. Some systems may experience a delayed AGN feedback (in particular at high redshift), allowing a massive CCA for a transient time (e.g. Phoenix cluster; McDonald et al. 2013).

### 6.3. $l_z$ distribution and radial profiles

At variance with the purely radiative run, the cold phase randomly condenses out of the  $l_z$  distribution shown in Fig. 3c (top), i.e. the cold clouds and filaments can be generated with both prograde and retrograde motions. Initially, the inner gas with lower  $l_z$  cools faster, growing a modest PDF (dark blue line). After 10 Myr, the wings of the broader PDF start to experience significant recurrent narrowing, as a result of violent collisions canceling angular momentum (occurring in a period of a few Myr). However, the mass of unaccreted cold gas tends to substantially rise with time (leading to a PDF with larger width and normalization), progressively obfuscating the previous effect. In the subsequent heated run (Fig. 5c), it will be easier to isolate the action of collisions, lacking the formation of a massive cooling flow.

An unbalance toward the right wing ( $l_z > 200 \text{ kpc km s}^{-1}$ ) persists due to the initial halo rotation, implying that a prograde (though clumpy) torus-like structure is a recurrent phenomenon. As  $Ta_t \ll 1$ , the role of rotation becomes negligible and the prograde bias disappears (GRO13). Conversely, as  $Ta_t > 3$ , the cold phase can only be generated with positive  $l_z$  (Fig. 3c, bottom) and the accretion follows that of the coherent thin disk (§4).

In Fig. 4d, the radial profiles are analogous to that found in GRO13, showing the massive condensation of warm/cold gas out of the hot phase via thermal instability, and the fluctuations imparted by turbulence. After full condensation, the cold gas typically populates the region within 3 kpc. Maximum density is slightly higher compared with GRO13 ( $n_e \sim 10^4 \text{ cm}^{-3}$ ), since the initial hydrostatic atmosphere has slightly shallower density gradient. The central X-ray temperature is flat, without a cuspy core, a characteristic mark of cold accretion dominating over the hot mode.

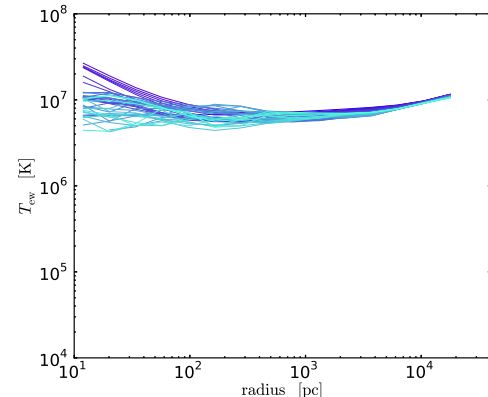
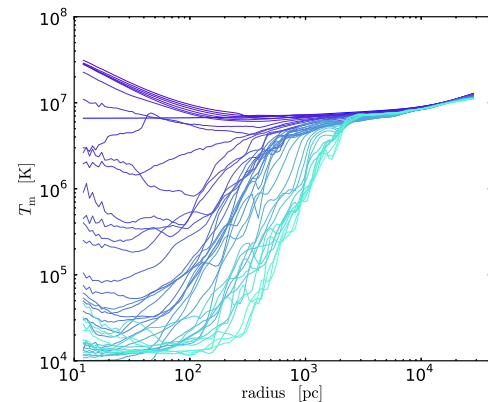
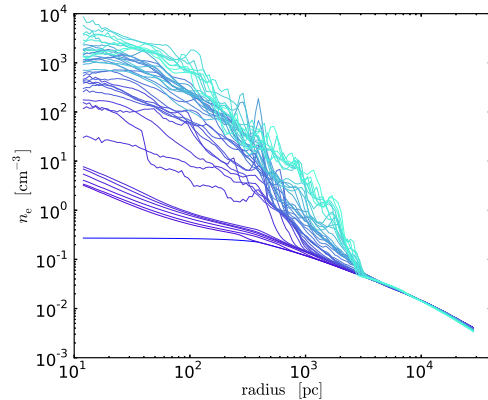


**Figure 4d.** Accretion with cooling, turbulence ( $Ma \sim 0.35$ ), and  $e_{\text{rot}} = 0.3$ : mass- and emission-weighted radial profiles of density and temperature (cf. Fig. 2c). The profiles show the condensation of warm/cold gas out of the hot phase via TI up to several kpc. The X-ray temperature is flat, with no cuspy core, a characteristic mark of cold accretion.

## 7. ACCRETION WITH HEATING, COOLING, AND TURBULENCE: CHAOTIC COLD ACCRETION

In the last set of models, we focus on the most frequent state for the hot plasma in a massive galaxy, group, or cluster. The cooling flow is now quenched via heating (§2.2) by 10–20 fold, in agreement with *XMM-Newton* observations (Tamura et al. 2003; Peterson & Fabian 2006). The source of heating can be mainly attributed to AGN feedback, albeit su-

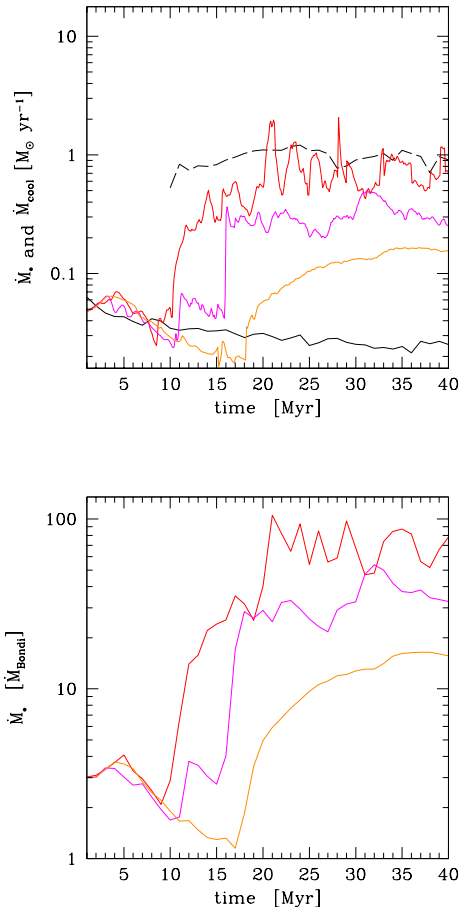


**Figure 5a.** Accretion with heating, cooling,  $e_{\text{rot}} = 0.3$ , and varying levels of turbulence: evolution of the accretion rate (the  $\dot{M}_*$  average in the top panel has 0.1 Myr step). The Mach number varies from the reference  $\text{Ma} \sim 0.35$  (red) to 1/2 (magenta) and 1/4 (orange) of this value, i.e.  $\text{Ta}_t \simeq 0.7, 1.5, 3$ , respectively. The dashed line is the average cooling rate (1 Myr step). As before, the solid black line is the adiabatic rotating model, and the run-time Bondi rate for the normalized plot is computed at  $r \sim 1\text{-}2$  kpc (§3). In the atmosphere with  $\text{Ta}_t < 1$ , chaotic cold accretion drives the dynamics, boosting the accretion rate up to  $100\times$  the Bondi rate, which is consistent with the non-rotating CCA evolution shown in GRO13. As  $\text{Ta}_t > 1$ , the accretion flow shifts from turbulence-driven (linked to extended filaments and boosted accretion) to rotationally-driven (tied to a coherent disk and suppressed accretion).

pernovae, thermal conduction, and mergers can possibly contribute.

### 7.1. Accretion rate

The key result is that, even in the presence of significant rotation ( $v_{\text{rot}} \approx 100 \text{ km s}^{-1}$ ), the accretion rate is boosted up to  $\sim 100\times$  the Bondi rate (Fig. 5a, red), which is consistent with the  $e_{\text{rot}} = 0$  model presented in GRO13 (sec. 7). The peaks in the accretion rate are comparable to the – now quenched<sup>5</sup>–cooling rate,  $\sim 1 M_{\odot} \text{ yr}^{-1}$  (dashed). Adopting  $\dot{M}_* \sim \dot{M}_{\text{cool}}$  is thus an effective subgrid accretion model for large-scale simulations and analytic calculations. Initially, accretion is in the regime driven by the rotating hot flow. After  $\sim 10$  Myr,

<sup>5</sup> We note star formation is observed to be inefficient in massive elliptical galaxies,  $\lesssim 1$  per cent of the pure cooling rate (e.g. McDonald et al. 2014).

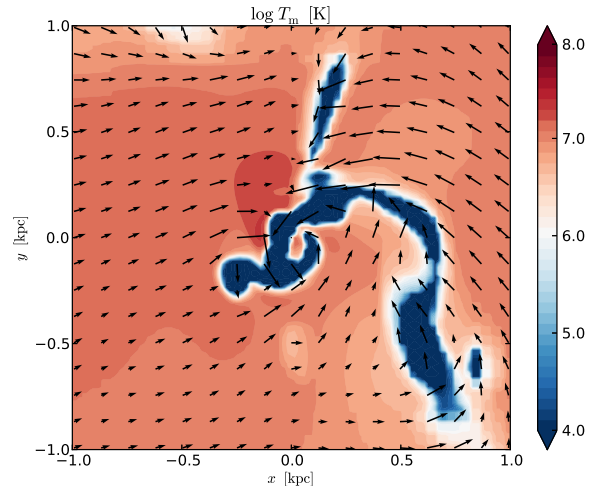


**Figure 5b.** Accretion with heating, cooling, turbulence ( $\text{Ma} \sim 0.35$ ), and  $e_{\text{rot}} = 0.3$ : temperature cross-section through  $z = 0$ , with the velocity field overlaid. Full circularization is not possible in a turbulent environment characterized by  $\text{Ta}_t < 1$ . The recurrent chaotic collisions between the cold filaments, clouds, and the inner volatile torus, cancel the angular momentum of the cold gas, leading to the rapid peaks in the accretion rate,  $\dot{M}_* \sim \dot{M}_{\text{cool}}$ . The convergence test is analogous to that presented in GRO13.

chaotic cold accretion drives the dynamics. At variance with §6, the presence of heating prevents the formation of a catastrophic cooling flow: the average  $\dot{M}_*$  and  $\dot{M}_{\text{cool}}$  do not increase with time. In the regions where  $t_{\text{cool}}/t_{\text{ff}} < 10$  (between  $r \sim 100$  pc and several kpc), thermal instability quickly grows in nonlinear way (see also Gaspari et al. 2012a), cold gas condenses out of the hot phase, and chaotic collisions promote the cancellation of angular momentum. As discussed in §1, multiwavelength observations support the TI and CCA scenario, detecting extended multiphase gas in the core of many massive galaxies, which is cospatial in X-ray, FUV, H $\alpha$ , and molecular band (e.g. McDonald et al. 2010, 2011; Werner et al. 2013, 2014).

CCA dominates as long as the following criterium is met:

$$\text{Ta}_t < 1. \quad (7)$$

In Fig. 5a, we show the models with 1/2 and 1/4 lower turbulence with respect to the reference  $\text{Ma} \sim 0.35$ , corresponding to  $\text{Ta}_t \sim 1.5$  (magenta) and 3 (orange), respectively. As the rotational velocity exceeds the turbulent velocity dispersion, the accretion rate is progressively suppressed by a factor  $\propto \text{Ta}_t$ . The accretion flow shifts from turbulence-driven, with chaotic filaments and boosted  $\dot{M}_*$ , to rotationally-driven, displaying a coherent disk and reduced  $\dot{M}_*$ . In the regime  $\text{Ta}_t \gg 1$ ,  $\dot{M}_*$  saturates around  $\sim 0.1 M_{\odot} \text{ yr}^{-1}$ , as perturbations induced by turbulence are not influencing the evolution of the thin disk.

In a complementary run (not shown), we doubled the rotational velocity ( $\approx 200 \text{ km s}^{-1}$ ) while fixing the reference  $\text{Ma} \sim 0.35$  (again  $\text{Ta}_t \sim 1.5$ ). The results are analogous to the previous models, after comparing identical cooling rate (stronger flattening implies higher densities at large radii, thereby larger cooling rates).

### 7.2. CCA dynamics and $l_z$ distribution

Chaotic cold accretion is mainly driven by the following physical processes. First, turbulence broadens the distribution of

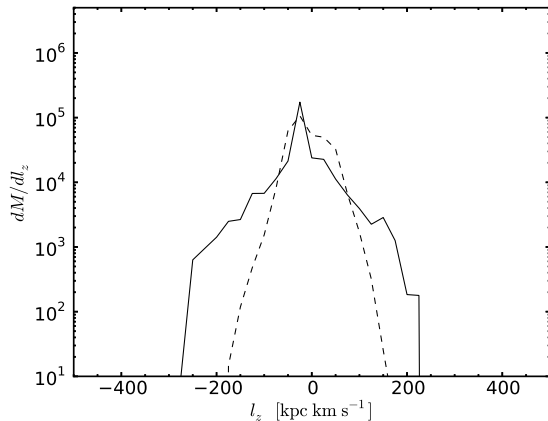


**Figure 5c.** Accretion with heating, cooling, turbulence ( $Ma \sim 0.35$ ), and  $e_{\text{rot}} = 0.3$ : mass PDF per bin of specific angular momentum  $l_z$ , for the cold phase (the hot phase has PDF analogous to Fig. 3c, top). After three rapid  $\dot{M}_\bullet$  bursts, the PDF narrows on average from 20 Myr (solid) to 27 Myr (dashed) due to major collisions canceling positive and negative  $l_z$ . The action of collisions is periodically contrasted by fresh condensation, favoring a broader distribution.

angular momentum related to the hot atmosphere, as shown in Fig. 3c (top; see discussion in §5.2). The broadening is  $\propto \sigma_v$  and induces both prograde and retrograde chaotic motions. By itself, the broadening of PDF( $l_z$ ) does not imply boosted accretion, since the hot gas is supported by pressure. The second step is the condensation of cold gas. The cooling gas retains the imprint of the hot phase, emerging out of the broad  $l_z$  distribution with both positive and negative values. During infall<sup>6</sup>, the clouds start to significantly collide, mainly in the inner 1 kpc (Fig. 5b), inducing major angular momentum cancellation (see also Pizzolato & Soker 2010). In Fig. 5c, we focus on the PDF( $l_z$ ) evolution between 20 and 27 Myr, as three major  $\dot{M}_\bullet$  bursts and collisions occur in rapid succession. Despite the continuous cold gas condensation, we observe a rapid narrowing of the  $l_z$  distribution, leading to the  $\dot{M}_\bullet$  bursts seen in Fig. 5a. At other times (not shown), gas condensation can regenerate one or both tails. Since the cooling rate and cold mass is quenched by over an order of magnitude compared with the pure cooling flow (consistently with observations; Tamura et al. 2003), collisional effects are not overwhelmed by condensation through time (as in the non-heated run; §6). The residual cold phase achieves a statistical steady state after  $\sim 2 t_{\text{cool}}$ , with no secular evolution, although shaped by recurrent cycles of broadening and narrowing of the angular momentum distribution.

Both turbulence and collisions characterize CCA. Without turbulence the angular momentum of the newborn cold phase would only have positive  $l_z$  (cf. Fig. 3c, bottom), leading to a coherent disk. Without collisions, the cold phase might not strongly boost accretion (no rapid  $l_z$  cancellation). Both processes are tightly related to  $\sigma_v$ . If  $Ta_t < 1$ , as in the reference run, turbulent diffusion dominates over the advection due to coherent rotation, leading to substantial PDF broadening and head-on cloud collisions. However, if  $Ta_t > 1$ , the broadening is too weak and collisions can not cancel angular momentum. The suppression in the accretion rate is relatively

<sup>6</sup> Nonlinear condensation is too fast and clouds are too massive to be directly affected by the driving, which is slowly injected at larger scale  $L$ .

smooth,  $\dot{M}_\bullet \propto Ta_t^{-1}$  (Fig. 5a), until the thin disk evolution dominates for  $Ta_t > 3$  (i.e. at least an order of magnitude in classic Taylor number; §1).

The linear transition can be crudely understood in terms of mixing length approximation. Accretion in a rotating atmosphere is ultimately limited by the diffusion time related to collisions (the PDF broadening, albeit directly tied to  $Ta_t$ , is the necessary but not sufficient condition). Using as effective collisional viscosity<sup>7</sup>  $\nu \sim \sigma_v \lambda$ , with  $\lambda$  the collisional mean free path, we can write the following scaling:

$$t_{\text{acc}} \approx t_{\text{diff}} \equiv \frac{r^2}{\nu} \sim \frac{v_{\text{rot}}}{\sigma_v} \frac{r}{\lambda} t_{\text{dyn}} \quad (8)$$

where we assumed the gas dynamical timescale is mainly associated with rotation. Clearly, the smaller the velocity dispersion, the longer the diffusion and hence accretion timescale. Typically, the clouds and filaments have to travel into the inner 1 kpc region to experience substantial collisions. Here, the mean free path is typically comparable to the radius (yet smaller than the global system), yielding the scaling  $t_{\text{acc}} \sim Ta_t t_{\text{dyn}}$ , in agreement with our findings (Fig. 5a). In general,  $\lambda$  varies depending on the size of the condensing clouds, which can be smaller than  $r$ . This slows the accretion time, creating the deeper valleys in  $\dot{M}_\bullet$ . Notice that, although the peaks in  $\dot{M}_\bullet$  are provided by major collisions, the average accretion rate is still  $\propto Ta_t^{-1}$ . CCA should be seen as a combination of major (e.g. Fig. 5b) and minor interactions (e.g. Fig. 16, GRO13), the former inducing more rapid  $l$  cancellation. As  $Ta_t < 1$ , turbulent diffusion overcomes rotation (Eq. 8 is no longer accurate) and the sinking of cold clouds – after condensing in a cooling time – occurs in a radial free-fall timescale, returning to the pure CCA presented in GRO13<sup>8</sup>.

The reference  $v_{\text{rot}} \approx 100 \text{ km s}^{-1}$  is near the high end of the realistic range (as we want to understand in clear way the impact of rotation). For  $e_{\text{rot}} > 0.3$ , the galaxy is substantially flattened and the gas  $v_{\text{rot}}$  would inconsistently exceed the stellar rotational velocity, commonly  $\sim 100 \text{ km s}^{-1}$  (Davies et al. 1983). Therefore, many massive elliptical galaxies should reside in the pure CCA regime ( $Ta_t \ll 1$ ), in particular after strong injection of turbulence, e.g. via AGN outbursts and merger events. On the other hand, some elliptical galaxies are observed to host central cold disks, which is a by-product of incomplete angular momentum cancellation, likely associated with  $Ta_t \gtrsim 3$  (e.g. Young et al. 2011; Alatalo et al. 2013) as turbulence and heating start to decrease (consistently with Table 1 and Figure 3 in Werner et al. 2014). Notice that, in the disk stage, AGN feedback can still be active (especially in galaxy clusters; Hamer et al. 2014; McNamara et al. 2014), albeit less episodic; only in the hot mode, the accretion rates and feedback are dramatically suppressed.

We note ram pressure drag is here secondary. The density contrast between the cold and hot phase is substantial,  $\rho_c/\rho_h \gtrsim 10^3$ . The cloud halting distance to lose all the kinetic energy can be estimated as  $d_{\text{halt}} \sim (e_{\text{kin},c}/\dot{e}_{\text{kin},c}) v_c \sim$

<sup>7</sup> Notice that CCA diffusivity, based on collisions and  $l$  cancellation, is different from the shear viscosity and associated steady inward/outward transport of  $l_z$  postulated in Keplerian thin disks (Shakura & Sunyaev 1973). In the latter model, the velocity is either prograde or retrograde only, and the cold rings experience friction due to internal micro-turbulence (e.g. driven by the magneto-rotational instability; Balbus & Hawley 1998).

<sup>8</sup> We note that the diffusivity due to turbulence ( $\sim Ma c_s L$ ) and collisions ( $\sim Ma c_s \lambda$ ) overcomes in all runs the numerical viscosity or the effective Shakura & Sunyaev viscosity (§4), since  $L, \lambda \gg \Delta x$ . This is corroborated by the convergence tests shown in GRO13 (sec. 7.5).

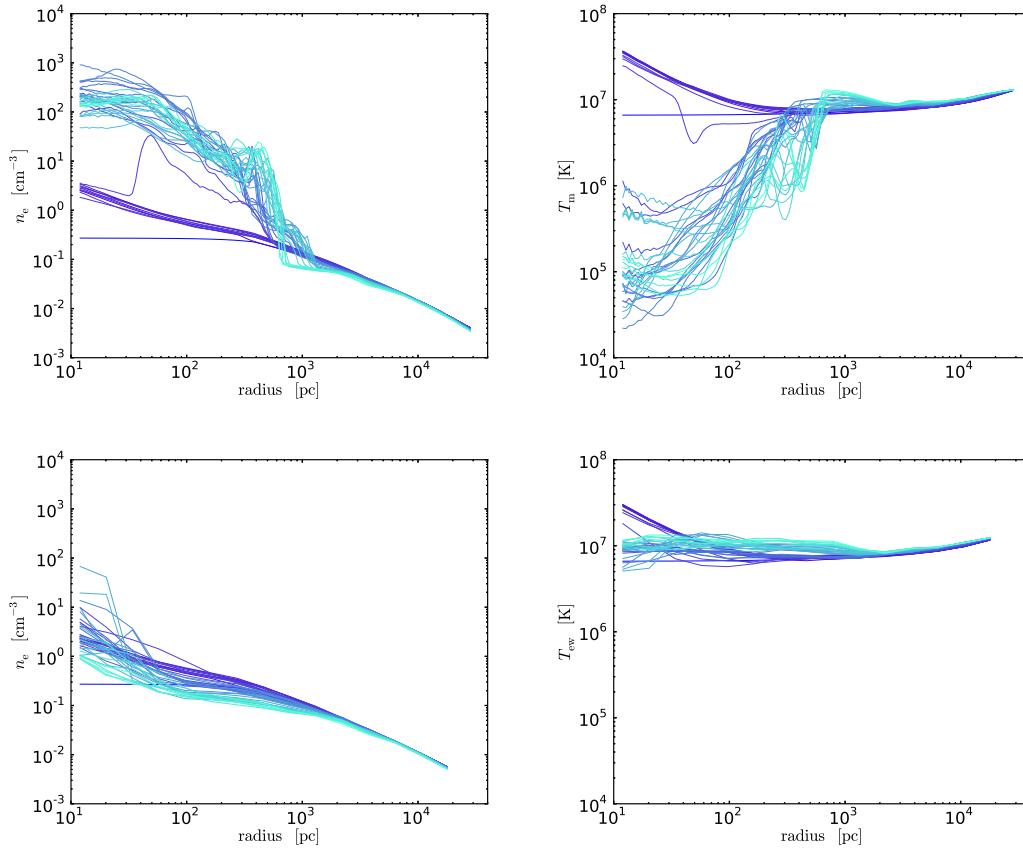


**Figure 5d.** Accretion with heating, cooling, turbulence ( $Ma \sim 0.35$ ), and  $e_{\text{rot}} = 0.3$ : 3D mass- (top) and X-ray emission-weighted (bottom) radial profiles of density and temperature (cf. Fig. 2c). The profiles show the extended multiphase structure, which is largely concealed in the X-ray band. The X-ray temperature profile is remarkably flat, in contrast with the hot-mode accretion, which has a peaked temperature profile. This is a key observable which can be thoroughly tested (e.g. Wong et al. 2014). The difference between the hot and cold phase density is typically 3 orders of magnitude. We note the thermodynamic mode is quasi isobaric since motions are subsonic (see also Gaspari et al. 2014b).

$(\rho_c/\rho_h)r_c$ , using  $e_{\text{kin},c} \sim \rho_c v_c^2 r_c^3$  and  $\dot{e}_{\text{kin},c} \sim F_{\text{drag}} v_c \sim (\rho_h v_c^2 r_c^2) v_c$ . Therefore, even small clouds of 50 pc would require distances larger than the box to lose most of its energy due to drag, while collisions occur in just a small fraction of the system size, mostly within  $r < 1$  kpc.

### 7.3. Radial profiles

The evolution of the  $t_{\text{cool}}/t_{\text{ff}}$  (TI-ratio) profiles is analogous to those presented in GRO13 (Fig. 15). The threshold  $\lesssim 10$  indicates the point where the condensation of extended cold gas is allowed (Gaspari et al. 2012a; McCourt et al. 2012; Sharma et al. 2012). Within the Bondi radius and above  $\sim 7$ -10 kpc thermal instability can not grow nonlinearly, as buoyancy dominates. Many cold clouds and filaments fill the region 200 pc - 1 kpc, where the ratio has a minimum around 4 and the initial gas density is above  $0.1 \text{ cm}^{-3}$ , leading to more rapid condensation. The funneling toward the BH allows more frequent interactions within this inner region. The dropout of cold gas results in a gradual increase of the average entropy and thus TI-ratio, as the plasma becomes more tenuous (in a later stage, feedback self-regulation prevents strong overheating; Gaspari et al. 2012a).

For systems with  $Ta_t > 1$ , the gas is mainly supported by coherent rotation during the condensation process, implying that radial compression is less relevant for the TI growth.

With no radially compressive term, it has been shown that the TI-ratio threshold is lower by an order of magnitude,  $t_{\text{cool}}/t_{\text{ff}} \lesssim 1$  (McCourt et al. 2012). Note that the free-fall time does not increase: the effective gravity is lower along  $R$ , but the cold gas tends to fall along the  $z$  direction and to settle on the equatorial plane, hence  $t_{\text{ff}}(z) = (2z/g(z))^{1/2}$  – which is identical to  $t_{\text{ff}}(r)$ . In other words, nonlinear TI and fragmented clouds are more difficult to form in a cooling gas shaped by the centrifugal force. This is confirmed by the  $Ta_t > 1$  runs, having a rather stable  $\dot{M}_\bullet$  evolution. Notice that  $t_{\text{cool}}/t_{\text{ff}} > 1$  does not imply that the cold phase will not form, but that the condensation is monolithic, leading to a disk-like structure, instead of filamentary (NGC 6868 and NGC 7049 are two examples; Werner et al. 2014). The reduced fragmentation also affects the  $Ta_t = 0.7$  run, favoring longer filaments instead of spherical clouds. The major cold phase interactions can be thus more prolonged inducing broader  $\dot{M}_\bullet$  peaks compared with GRO13.

The mass-weighted radial profiles (Fig. 5d, top panels) highlight the extended multiphase structure and time-dependent nature of the accretion flow. The extension of multiphase filaments up to a few kpc is consistent with  $H\alpha$  observations (Fig. 1 in Werner et al. 2014). Performing an X-ray observation (bottom panels) instead conceals them, allowing the hot component to emerge ( $T > 0.3 \text{ keV}$ ). As in

GRO13, the X-ray emission-weighted temperature profile is remarkably flat, in contrast with the peaked profile of the adiabatic flow (Fig. 3d). This is a key observable and prediction which can be tested, in particular with future X-ray missions (e.g. *Athena*). Recently, the Megasecond *Chandra* observation of NGC 3115 (Wong et al. 2014) has discovered a flat temperature core with multiphase structure within the Bondi radius. Their retrieved density profile within the inner 200 pc has moderate slope of -1, consistent with our findings (bottom left panel).

The mass-weighted density profiles point out that an inner ( $r \lesssim 100$  pc) clumpy torus is relatively common, though continuously formed and dismantled by the chaotic dynamics. The presence of an inner obscuring torus is supported by extensive AGN literature (Bianchi et al. 2012 for a review). The central volatile structure derives from the accumulation of multiple filaments, which have not yet completely canceled angular momentum. On the other hand, its rising cross-section increases the collisional rate with the incoming clouds, promoting efficient angular momentum cancellation. The PDF( $l_z$ ) for the cold gas within 100 pc is self-similar to Fig. 5c, continuously broadening (either one or two tails) and narrowing through time, albeit in a smaller range,  $|l_z| < 40$  kpc km s<sup>-1</sup> (i.e. below circular angular momentum at 100 pc). As  $Ta_t > 1$ , collisions become less efficient (Eq. 8), and the torus can stabilize in a more coherent and extended disk.

Another interesting result is that the cold phase temperature can fluctuate between  $10^4 - 10^5$  K, implying that, in a heated and chaotic environment, the cooling gas does not have to necessarily collapse to the floor (or molecular) temperature, but it can remain relatively warm. Multi-wavelength data also indicate that cold filaments have a complex warm transition layer (e.g. McDonald & Veilleux 2009; McDonald et al. 2010, 2011). A possible explanation is related to the fact that subsonic turbulence in the hot phase becomes supersonic through the cold medium, thus increasing the efficiency of both turbulent mixing and dissipation, consequently reheating the filaments. The observed ionized gas within central filaments frequently shows significant velocity dispersions ( $\sim 100$  km s<sup>-1</sup>; e.g. Canning et al. 2014; Werner et al. 2014), supporting this model. We will explore in depth the evolution of single cold filaments and collisions with future simulations implementing additional physics (e.g. magnetic fields and anisotropic conduction) and higher local resolution.

## 8. SUMMARY & CONCLUSIONS

We carried out 3D high-resolution simulations to perform controlled astrophysical experiments of the accretion flow on to a supermassive black hole, resolving the galactic 50 kpc scale down to the inner sub-pc scale. We gradually increased the realistic complexity of the hydrodynamic flow, including cooling, turbulence, and heating. In this work, we focused on the role of rotation in altering accretion (reference  $e_{rot} = 0.3$ , i.e.  $v_{rot} \approx 100$  km s<sup>-1</sup>), in comparison with the non-rotating models presented in Gaspari et al. 2013b (GRO13). The main features of each accretion flow can be summarized as follows.

- *Adiabatic rotating flow.*

The hot pressure-dominated flow forms a central rotational barrier ( $\lesssim r_B$ ), with a thick toroidal geometry and mild variability. The gas can only accrete along a

polar funnel with half-opening angle  $\sim \pi/4$ . Compared with the spherically symmetric model, the accretion rate is suppressed by a characteristic factor of  $\sim 3$ . The accretion rate is comparable to the reference  $\dot{M}_{Bondi}$  computed at  $r \sim 1-2$  kpc. The stratification of the atmosphere slightly decreases the central density and accretion through time. The characteristic mark of the hot flow is the cuspy (X-ray or mass-weighted) temperature profile. The coherent prograde rotation preserves the initial positive angular momentum distribution.

- *Radiative rotating flow.*

The radiatively cooling gas loses pressure support in a cooling time and circularizes on the equatorial plane, forming a cold thin disk. At variance with the classic cooling flow, the accretion rate is suppressed and decoupled from the cooling rate,  $\dot{M}_\bullet \lesssim 10^{-2} \dot{M}_{cool}$ . However,  $\dot{M}_\bullet$  is still a decade higher compared with the adiabatic flow due to the halo condensation. The cold phase progressively accumulates higher positive  $l_z$ , as the kpc-size disk grows through time via condensation.

- *Adiabatic rotating flow stirred by turbulence.*

From the perspective of the accretion rate and  $\rho$ ,  $T$  radial profiles, the stirred hot flow is analogous to the unperturbed adiabatic evolution, with increased variability (factor of 2). The similar  $\sim 1/3$  suppression of  $\dot{M}_\bullet$  is due to the fact that subsonic turbulence is tied to local gas vorticity (further enhanced by the baroclinic instability in a stratified medium). As  $Ta_t \equiv v_{rot}/\sigma_v < 1$ , the  $l_z$  distribution is reshaped and substantially broadened via turbulent diffusion, generating both prograde and retrograde eddies. If  $Ta_t > 1$ , the initial PDF is only slightly modified: the flow is again driven and suppressed by coherent rotation ( $l_z > 0$ ) and not by the turbulent eddies.

- *Chaotic cold accretion (cooling, heating, turbulence).*

As long as  $Ta_t < 1$ , chaotic cold accretion (CCA) drives the dynamics, as found in GRO13. Within several kpc, thermal instability can grow nonlinearly ( $t_{cool}/t_{ff} < 10$ ), extended multi-temperature filaments condense out of the hot phase and rain toward the BH. The collisions ( $r < 1$  kpc) between the cold clouds, filaments, and central clumpy torus allow to efficiently cancel angular momentum, boosting the accretion rate, with impulsive peaks up to the cooling rate or  $100\times$  the Bondi rate. Using  $\dot{M}_\bullet \sim \dot{M}_{cool}$  is thus a realistic (subgrid) model for large-scale simulations and analytic studies. Without heating, the CCA evolution is analogous, albeit the cold phase properties (cold mass, collisions, PDF) are magnified by an order magnitude.

The condensed cold phase retains the imprint of the stirred hot phase, emerging out of the broadened  $l_z$  distribution. The presence of both prograde and retrograde motions permits the cancellation of angular momentum. After major collisions the PDF narrows ( $\dot{M}_\bullet$  peaks), while condensation broadens it again. Transient incomplete cancellation ( $\dot{M}_\bullet$  valleys) creates

a clumpy, highly variable torus, later favoring the interactions with incoming clouds. In the regime  $Ta_t > 1$ , turbulent diffusion becomes weaker than advection due to rotation, reducing the relative PDF broadening and the efficiency of collisions. The accretion rate thus decreases as  $Ta_t^{-1}$ , until the cold disk drives again the evolution. This is aggravated by the increased difficulty of TI and fragmented clouds to form under coherent rotation, as the thermal instability threshold is lowered due to the reduced influence of radial compression.

The present work, together with GRO13, emphasizes the central role of chaotic cold accretion in the evolution of (supermassive) black holes, also in the presence of rotation. The high and variable accretion rates,  $\dot{M}_\bullet \sim \dot{M}_{cool}$ , can trigger the required level and self-regulation of the AGN feedback, in order to quench cooling flows, star formation, and to shape the observed thermodynamic properties of massive galaxies, groups, and clusters (e.g. Gaspari et al. 2011a,b, 2012a,b; §1).

The results obtained through the last years corroborate the following cosmic accretion/feedback cycle affecting gaseous halos. As gas cooling starts to dominate over heating ( $t_{cool}/t_{ff} < 10$  or central entropy  $K_0 \lesssim 20$  keV cm<sup>2</sup>), CCA is triggered<sup>9</sup>, boosting the accretion rate ( $\dot{M}_\bullet \gg \dot{M}_{Bondi}$ ) and consequently the feedback injection via AGN outflows/jets ( $Ta_t < 1$ ). This phase can be observationally probed via the flat X-ray temperature profile and multiwavelength extended filaments (e.g. McDonald et al. 2010, 2011; Werner et al. 2013; Wong et al. 2014). As the core entropy rises and turbulence diminishes ( $Ta_t > 1$ ), nonlinear TI weakens and the rotating disk remains the only residual cold entity (e.g. Mathews & Brighenti 2003; Young et al. 2011; Alatalo et al. 2013; NGC 6868 and NGC 7049 in Werner et al. 2014). The transition is associated with a gradual decrease in the accretion rate  $\propto Ta_t^{-1}$  (feedback can still be active). Waiting longer times, as the disk is consumed (e.g. via accretion or star formation) and the halo has been overheated by feedback, the hot gas is the only resource available to poorly fuel the black hole ( $t_{cool}/t_{ff} \gg 10$ ). The main diagnostic of this hot-mode regime is the cuspy X-ray temperature profile (cf. Humphrey et al. 2009), typically associated with more quiescent systems (e.g. NGC 4649; Humphrey et al. 2008). Transitioning from the fully cold mode to hot mode, the accretion rate experiences a strong suppression, from  $100\times$  to a small fraction of the Bondi rate. Feedback heating becomes negligible, entropy starts to decrease, and the gaseous halo is allowed to cool again, restarting a new cycle: CCA/boosted feedback  $\rightarrow$  rotating disk  $\rightarrow$  hot mode/suppressed feedback.

Forthcoming observations of cold gas combining several wavelengths, e.g. via *Herschel*, HST, SOAR, CARMA, SKA, and the newly expanding ALMA observatory, will be instrumental to better probe chaotic cold accretion and the related predictions. Besides improving the sample size, the new data should be able to shed light on key astrophysical questions, as the amount of cold gas ‘raining’ on to the black hole, the kinematics of the cold phase (filaments, clouds, rotating disk), and its coupling with AGN feedback.

<sup>9</sup> A non-zero level of subsonic turbulence is always present in real systems (§2.2), e.g. due to galaxy motions, mergers, stellar evolution. The initial AGN outburst also generates further turbulence.

#### ACKNOWLEDGMENTS

The FLASH code was in part developed by the DOE NNSA-ASC OASCR Flash center at the University of Chicago. M.G. is grateful for the financial support provided by the Max Planck Fellowship. M.R. acknowledges NSF grant AST 1008454 and NASA ATP grant 12-ATP12-0017. S.P.O. acknowledges NASA grant NNX12AG73G. F.B. is in part supported by the Prin MIUR grant 2010LY5N2T. High-performance computing resources were provided by the NASA/Ames HEC Program (SMD-13-4373, SMD-13-4377, SMD-14-4819; Pleiades) and by the CLS center. The post-processing analysis was in part performed with YT (Turk et al. 2011).

#### REFERENCES

- Alatalo, K., Davis, T. A., Bureau, M., et al. 2013, MNRAS, 432, 1796  
 Allen, S. W., Dunn, R. J. H., Fabian, A. C., Taylor, G. B., & Reynolds, C. S. 2006, MNRAS, 372, 21  
 Anderson, M. E., & Bregman, J. N. 2011, ApJ, 737, 22  
 Anderson, M. E., Bregman, J. N., & Dai, X. 2013, ApJ, 762, 106  
 Baganoff, F. K., Maeda, Y., Morris, M., et al. 2003, ApJ, 591, 891  
 Bakes, E. L. O., & Tielens, A. G. G. M. 1994, ApJ, 427, 822  
 Balbus, S. A., & Hawley, J. F. 1998, Reviews of Modern Physics, 70, 1  
 Balbus, S. A., & Soker, N. 1989, ApJ, 341, 611  
 Banerjee, N., & Sharma, P. 2014, MNRAS, 443, 687  
 Barai, P., Proga, D., & Nagamine, K. 2012, MNRAS, 424, 728  
 Barai, P., Viel, M., Murante, G., Gaspari, M., & Borgani, S. 2014, MNRAS, 437, 1456  
 Best, P. N., von der Linden, A., Kauffmann, G., Heckman, T. M., & Kaiser, C. R. 2007, MNRAS, 379, 894  
 Bianchi, S., Maiolino, R., & Risaliti, G. 2012, ADA&A, 2012, arXiv:1201.2119  
 Binney, J. J., Davies, R. L., & Illingworth, G. D. 1990, ApJ, 361, 78  
 Bois, M., Emsellem, E., Bournaud, F., et al. 2011, MNRAS, 416, 1654  
 Bondi, H. 1952, MNRAS, 112, 195  
 Bondi, H., & Hoyle, F. 1944, MNRAS, 104, 273  
 Booth, C. M., & Schaye, J. 2009, MNRAS, 398, 53  
 Borgani, S., & Kravtsov, A. 2011, Advanced Science Letters, 4, 204  
 Bregman, J. N., Fabian, A. C., Miller, E. D., & Irwin, J. A. 2006, ApJ, 642, 746  
 Brighenti, F., & Mathews, W. G. 1996, ApJ, 470, 747  
 —. 1999, ApJ, 512, 65  
 —. 2000, ApJ, 539, 675  
 —. 2003, ApJ, 587, 580  
 Brighenti, F., Mathews, W. G., Humphrey, P. J., & Buote, D. A. 2009, ApJ, 705, 1672  
 Canning, R. E. A., Sun, M., Sanders, J. S., et al. 2013, MNRAS, 435, 1108  
 Canning, R. E. A., Ryon, J. E., Gallagher, III, J. S., et al. 2014, ArXiv e-prints, arXiv:1406.4800  
 Caon, N., Macchetto, D., & Pastoriza, M. 2000, ApJS, 127, 39  
 Cattaneo, A., & Teyssier, R. 2007, MNRAS, 376, 1547  
 Cattaneo, A., Faber, S. M., Binney, J., et al. 2009, Nature, 460, 213  
 Cavagnolo, K. W., Donahue, M., Voit, G. M., & Sun, M. 2008, ApJ, 683, L107  
 Churazov, E., Forman, W., Vikhlinin, A., et al. 2008, MNRAS, 388, 1062  
 Churazov, E., Sunyaev, R., Forman, W., & Böhringer, H. 2002, MNRAS, 332, 729  
 Crawford, C. S., Allen, S. W., Ebeling, H., Edge, A. C., & Fabian, A. C. 1999, MNRAS, 306, 857  
 Croton, D. J., Springel, V., White, S. D. M., et al. 2006, MNRAS, 365, 11  
 Dai, X., Anderson, M. E., Bregman, J. N., & Miller, J. M. 2012, ApJ, 755, 107  
 David, L. P., Lim, J., Forman, W., et al. 2014, ArXiv e-prints, arXiv:1407.3235  
 Davies, R. L., Efstathiou, G., Fall, S. M., Illingworth, G., & Schechter, P. L. 1983, ApJ, 266, 41  
 de Plaa, J., Zhuravleva, I., Werner, N., et al. 2012, A&A, 539, A34  
 Dekel, A., Birnboim, Y., Engel, G., et al. 2009, Nature, 457, 451  
 Di Matteo, T., Allen, S. W., Fabian, A. C., Wilson, A. S., & Young, A. J. 2003, ApJ, 582, 133  
 Di Matteo, T., Springel, V., & Hernquist, L. 2005, Nature, 433, 604  
 Diehl, S., & Statler, T. S. 2007, ApJ, 668, 150  
 —. 2008, ApJ, 687, 986

- Dolag, K., Vazza, F., Brunetti, G., & Tormen, G. 2005, *MNRAS*, 364, 753
- Edge, A. C. 2001, *MNRAS*, 328, 762
- Elmegreen, B. G., & Scalo, J. 2004, *ARA&A*, 42, 211
- Emsellem, E., Cappellari, M., Krajnović, D., et al. 2007, *MNRAS*, 379, 401  
— 2011, *MNRAS*, 414, 888
- Field, G. B. 1965, *ApJ*, 142, 531
- Fisher, R. T., Kadanoff, L. P., Lamb, D. Q., et al. 2008, *IBM J. Res. & Dev.*, 52, 127
- Fryxell, B., Olson, K., Ricker, P., et al. 2000, *ApJS*, 131, 273
- Fujita, Y., Kawakatu, N., & Shlosman, I. 2014, *ArXiv e-prints*, arXiv:1406.6366
- Gaspari, M., Ruszkowski, M., & Sharma, P. 2012a, *ApJ*, 746, 94
- Gaspari, M., Brighenti, F., & Temi, P. 2012b, *MNRAS*, 424, 190
- Gaspari, M., Brighenti, F., & Ruszkowski, M. 2013a, *Astronomische Nachrichten*, 334, 394
- Gaspari, M., Brighenti, F., Temi, P., & Etori, S. 2014a, *ApJ*, 783, L10
- Gaspari, M., & Churazov, E. 2013, *A&A*, 559, A78
- Gaspari, M., Churazov, E., Nagai, D., Lau, E. T., & Zhuravleva, I. 2014b, arXiv:astro-ph/1404.5302, arXiv:1404.5302
- Gaspari, M., Ruszkowski, M., & Oh, S. P. 2013b, *MNRAS*, 432, 3401
- Gaspari, M., Melioli, C., Brighenti, F., & D’Ercole, A. 2011a, *MNRAS*, 411, 349
- Gaspari, M., Brighenti, F., D’Ercole, A., & Melioli, C. 2011b, *MNRAS*, 415, 1549
- Hamer, S. L., Edge, A. C., Swinbank, A. M., et al. 2014, *MNRAS*, 437, 862
- Hardcastle, M. J., Evans, D. A., & Croston, J. H. 2007, *MNRAS*, 376, 1849
- Hatch, N. A., Crawford, C. S., Fabian, A. C., & Johnstone, R. M. 2005, *MNRAS*, 358, 765
- Heckman, T. M., Baum, S. A., van Breugel, W. J. M., & McCarthy, P. 1989, *ApJ*, 338, 48
- Hobbs, A., Nayakshin, S., Power, C., & King, A. 2011, *MNRAS*, 413, 2633
- Hopkins, P. F., Narayan, R., & Hernquist, L. 2006, *ApJ*, 643, 641
- Hopkins, P. F., & Quataert, E. 2010, *MNRAS*, 407, 1529  
— 2011, *MNRAS*, 415, 1027
- Humphrey, P. J., Buote, D. A., Brighenti, F., Gebhardt, K., & Mathews, W. G. 2008, *ApJ*, 683, 161  
— 2009, *ApJ*, 703, 1257
- Jaffe, W., Bremer, M. N., & Baker, K. 2005, *MNRAS*, 360, 748
- Jimmy, Tran, K.-V., Brough, S., et al. 2013, *ApJ*, 778, 171
- Kim, J., & Ryu, D. 2005, *ApJ*, 630, L45
- King, A. R., & Pringle, J. E. 2006, *MNRAS*, 373, L90  
— 2007, *MNRAS*, 377, L25
- Kormendy, J., Fisher, D. B., Cornell, M. E., & Bender, R. 2009, *ApJS*, 182, 216
- Krolik, J. H., & London, R. A. 1983, *ApJ*, 267, 18
- Krumholz, M. R., McKee, C. F., & Klein, R. I. 2005, *ApJ*, 618, 757  
— 2006, *ApJ*, 638, 369
- Lau, E. T., Kravtsov, A. V., & Nagai, D. 2009, *ApJ*, 705, 1129
- Lim, J., Leon, S., Combes, F., & Dinh-V-Trung. 2000, *ApJ*, 545, L93
- Loewenstein, M., Mushotzky, R. F., Angelini, L., Arnaud, K. A., & Quataert, E. 2001, *ApJ*, 555, L21
- Macchetto, F., Pastoriza, M., Caon, N., et al. 1996, *A&AS*, 120, 463
- Markevitch, M., & Vikhlinin, A. 2007, *Phys. Rep.*, 443, 1
- Mathews, W. G., & Brighenti, F. 2003, *ARA&A*, 41, 191
- Mathews, W. G., & Guo, F. 2012, *ApJ*, 754, 154
- McCarthy, I. G., Babul, A., Bower, R. G., & Balogh, M. L. 2008, *MNRAS*, 386, 1309
- McCourt, M., Sharma, P., Quataert, E., & Parrish, I. J. 2012, *MNRAS*, 419, 3319
- McDonald, M., Benson, B., Veilleux, S., Bautz, M. W., & Reichardt, C. L. 2013, *ApJ*, 765, L37
- McDonald, M., Roediger, J. C., Veilleux, S., & Ehlert, S. 2014, *ArXiv e-prints*, arXiv:1407.4461
- McDonald, M., & Veilleux, S. 2009, *ApJ*, 703, L172
- McDonald, M., Veilleux, S., & Mushotzky, R. 2011, *ApJ*, 731, 33
- McDonald, M., Veilleux, S., & Rupke, D. S. N. 2012, *ApJ*, 746, 153
- McDonald, M., Veilleux, S., Rupke, D. S. N., & Mushotzky, R. 2010, *ApJ*, 721, 1262
- McNamara, B. R., & Nulsen, P. E. J. 2007, *ARA&A*, 45, 117  
— 2012, *New Journal of Physics*, 14, 055023
- McNamara, B. R., Russell, H. R., Nulsen, P. E. J., et al. 2014, *ApJ*, 785, 44
- Mittal, R., Hudson, D. S., Reiprich, T. H., & Clarke, T. 2009, *A&A*, 501, 835
- Mittal, R., Oonk, J. B. R., Ferland, G. J., et al. 2012, *MNRAS*, 426, 2957
- Nagai, D., Vikhlinin, A., & Kravtsov, A. V. 2007, *ApJ*, 655, 98
- Narayan, R., & Fabian, A. C. 2011, *MNRAS*, 415, 3721
- Nayakshin, S., & King, A. 2007, *ArXiv e-prints*, arXiv:0705.1686
- Nemmen, R. S., & Tchekhovskoy, A. 2014, *ArXiv e-prints*, arXiv:1406.7420
- Norman, M. L., & Bryan, G. L. 1999, in *Lecture Notes in Physics*, Berlin Springer Verlag, Vol. 530, *The Radio Galaxy Messier 87*, ed. H.-J. Röser & K. Meisenheimer, 106
- Oonk, J. B. R., Jaffe, W., Bremer, M. N., & van Weeren, R. J. 2010, *MNRAS*, 405, 898
- Paczyński, B., & Wiita, P. J. 1980, *A&A*, 88, 23
- Peterson, J. R., & Fabian, A. C. 2006, *Phys. Rep.*, 427, 1
- Pinkney, J., Gebhardt, K., Bender, R., et al. 2003, *ApJ*, 596, 903
- Pizzolato, F., & Soker, N. 2005, *ApJ*, 632, 821  
— 2010, *MNRAS*, 408, 961
- Planck Collaboration, Ade, P. A. R., Aghanim, N., et al. 2013, *A&A*, 557, A52
- Proga, D., & Begelman, M. C. 2003, *ApJ*, 582, 69
- Quataert, E., & Narayan, R. 2000, *ApJ*, 528, 236
- Rafferty, D. A., McNamara, B. R., & Nulsen, P. E. J. 2008, *ApJ*, 687, 899
- Rafferty, D. A., McNamara, B. R., Nulsen, P. E. J., & Wise, M. W. 2006, *ApJ*, 652, 216
- Rasmussen, J., & Ponman, T. J. 2009, *MNRAS*, 399, 239
- Reynolds, C. S., Di Matteo, T., Fabian, A. C., Hwang, U., & Canizares, C. R. 1996, *MNRAS*, 283, L111
- Russell, H. R., McNamara, B. R., Edge, A. C., et al. 2014, *ApJ*, 784, 78
- Ruszkowski, M., & Oh, S. P. 2010, *ApJ*, 713, 1332  
— 2011, *MNRAS*, 414, 1493
- Salomé, P., & Combes, F. 2003, *A&A*, 412, 657
- Salomé, P., Combes, F., Revaz, Y., et al. 2008, *A&A*, 484, 317
- Sanders, J. S., & Fabian, A. C. 2013, *MNRAS*, 429, 2727
- Schuecker, P., Finoguenov, A., Miniati, F., Böhringer, H., & Briel, U. G. 2004, *A&A*, 426, 387
- Shabala, S. S., Ash, S., Alexander, P., & Riley, J. M. 2008, *MNRAS*, 388, 625
- Shakura, N. I., & Sunyaev, R. A. 1973, *A&A*, 24, 337
- Sharma, P., McCourt, M., Quataert, E., & Parrish, I. J. 2012, *MNRAS*, 420, 3174
- Sijacki, D., Springel, V., Di Matteo, T., & Hernquist, L. 2007, *MNRAS*, 380, 877
- Soker, N. 2006, *NewA*, 12, 38
- Soker, N., Sternberg, A., & Pizzolato, F. 2009, in *American Institute of Physics Conference Series*, Vol. 1201, *American Institute of Physics Conference Series*, ed. S. Heinz & E. Wilcots, 321–325
- Sparks, W. B., Pringle, J. E., Carswell, R. F., et al. 2012, *ApJ*, 750, L5
- Springel, V., Di Matteo, T., & Hernquist, L. 2005, *MNRAS*, 361, 776
- Strickland, D. K., & Stevens, I. R. 2000, *MNRAS*, 314, 511
- Sun, M., Voit, G. M., Donahue, M., et al. 2009, *ApJ*, 693, 1142
- Sutherland, R. S., & Dopita, M. A. 1993, *ApJS*, 88, 253
- Tamura, T., Kaastra, J. S., Makishima, K., & Takahashi, I. 2003, *A&A*, 399, 497
- Turk, M. J., Smith, B. D., Oishi, J. S., et al. 2011, *ApJS*, 192, 9
- Vazza, F., Brunetti, G., Kritsuk, A., et al. 2009, *A&A*, 504, 33
- Vikhlinin, A., Kravtsov, A., Forman, W., et al. 2006, *ApJ*, 640, 691
- Werner, N., Oonk, J. B. R., Canning, R. E. A., et al. 2013, *ApJ*, 767, 153
- Werner, N., Oonk, J. B. R., Sun, M., et al. 2014, *MNRAS*, 439, 2291
- Wilman, R. J., Edge, A. C., McGregor, P. J., & McNamara, B. R. 2011, *MNRAS*, 416, 2060
- Wilman, R. J., Edge, A. C., & Swinbank, A. M. 2009, *MNRAS*, 395, 1355
- Wong, K.-W., Irwin, J. A., Shcherbakov, R. V., et al. 2014, *ApJ*, 780, 9
- Young, L. M., Bureau, M., Davis, T. A., et al. 2011, *MNRAS*, 414, 940
- Zabludoff, A. I., Geller, M. J., Huchra, J. P., & Ramella, M. 1993, *AJ*, 106, 1301
- ZuHone, J. A., Markevitch, M., Ruszkowski, M., & Lee, D. 2013, *ApJ*, 762, 69